

The efficient cluster packing model – An atomic structural model for metallic glasses

D.B. Miracle *

Air Force Research Laboratory, Materials and Manufacturing Directorate, 2230 Tenth Street, Wright-Patterson AFB, OH 45433-7817, USA

Received 17 June 2005; received in revised form 9 June 2006; accepted 15 June 2006

Available online 7 August 2006

Abstract

A structural model is described for metallic glasses based on a new sphere packing scheme – the efficient filling of space by solute-centered clusters. This model combines random positioning of solvent atoms with atomic order of solutes. It shows that metallic glasses contain ≤ 4 topologically distinct species and that solutes possess specific sizes relative to solvent atoms to produce efficient atomic packing. Validation is achieved by quantitative predictions of nearest-neighbor partial coordination numbers, medium-range solute ordering, density and metallic glass topologies. Good agreement is achieved in each of these areas. This model is able to reproduce compositions for a broad range of metallic glasses, provides specific guidance for the exploration of new bulk metallic glasses and may give new insights into other metallic glass studies. The new scheme introduced here for the efficient filling of space in extended systems of unequal spheres may have relevance to other fields.

© 2006 Acta Materialia Inc. Published by Elsevier Ltd. All rights reserved.

Keywords: Metallic glasses; Atomic structure; Modeling

1. Introduction

Over the past 45 years, metallic glasses have grown from a singular observation [1] to an expansive class of alloys with broad scientific and commercial importance. The exceptional physical, chemical, magnetic and mechanical properties of metallic glasses have enabled applications that include low loss magnetic transformer cores, corrosion resistant coatings, golf club heads and structural hinges for digital micromirror devices. It is unusual that this progress has been accomplished without the benefit of an atomic structural model. Engineered materials require a strict balance between properties, which in turn requires a robust understanding of structure. The foundation for this understanding in crystalline solids is an accurate and complete atomic structural model consisting of a simple and precise local representative structural element (unit cell) that possesses long-range translational periodicity. Models for opti-

cal, thermal, electrical, physical and mechanical properties are based upon an underlying knowledge of this structure. Well-defined local representative structural elements (RSEs) such as SiO_4 or BO_3 polyhedra are established in structural models for oxide glasses. Although periodicity is absent in these glasses, the arrangement between adjacent polyhedra is established [2], providing a basis for a statistical structural description. An approach has recently been proposed for defining specific local atomic configurations in metallic glasses [3], but rules for extending a structural description beyond the nearest neighbor shell have not been developed in detail.

Research over the past four decades provides an extensive database that firmly establishes the characteristics of metallic glasses. These characteristics give insight into the atomic structure and provide constraints against which a structural model can be constructed and assessed. For example, in addition to randomness as the defining structural feature, diffraction shows short-range atomic order (SRO) [4–15] and a surprising degree of medium range atomic order (MRO) [5,16–18]. The observation that bulk

* Tel.: +1 937 255 3007.

E-mail address: Daniel.miracle@wpafb.af.mil.

metallic glasses have densities that are only marginally lower than the same alloys in the crystalline state [19–22] suggests that atomic packing is efficient over all length scales. This is corroborated by the result that the best glass forming compositions correspond to a minimum in molar volume [23–26] or the lowest volume change upon solidification [20,21,26,27]. An approach for quantifying local atomic packing shows that packing is very efficient around both solute and solvent atoms [28], further supporting this idea. Relative atomic size has long been known to be important [24,29–32], and experience shows that metallic glasses are obtained when solutes have atomic radii that differ from the solvent by at least 12% [29,32]. A recent refinement has shown that solutes with specific radii relative to the solvent species are preferred [3]. The best metallic glasses are generally obtained in alloys that have three or more solute species [32], and distinct relationships have been observed between solute sizes and concentrations [33–35]. A critical solute concentration destabilizes the competing crystalline supersaturated solid solution relative to the undercooled liquid [30]. It is empirically observed that glass formability is extremely sensitive to the concentrations of some elements but is notably insensitive to the concentrations of other elements. Finally, it is generally observed that systems with a large negative heat of mixing provide the best glass forming alloys [24,32].

Summarizing these observations, the atomic structure of metallic glasses is characterized not only by randomness but also by SRO, MRO and efficient atomic packing around both solute and solvent atoms. Broad boundaries exist for the number, relative sizes and concentrations of solutes. Finally, a chemical or thermodynamic contribution to stability exists through a large negative enthalpy of mixing. A credible structural model must be consistent with these established features as a minimum criterion for acceptance, and a convincing structural model will provide a predictive capability for many of these features.

A strong case has been made for solute-centered atomic clusters as local RSEs. A tri-capped trigonal prism was first proposed to represent transition metal–metalloid glasses [5,36–38], and icosahedral clusters have been added as likely RSEs based on experiments [11,14,15,39–42] and computer simulations [43–45]. Geometric considerations of efficient local atomic packing (ELAP) have recently expanded the list of candidate clusters that may exist as local RSEs in metallic glasses [3,46–48]. However, these earlier works provide no detailed approach for extending structure beyond the nearest neighbor shell in a manner that is consistent with the experimentally established characteristics of metallic glasses described above.

The purpose of this paper is to present a detailed atomic structural model for metallic glasses that is consistent with each of the characteristics described above. Initial concepts outlined in [47] are extended here to give a complete model description. New analyses are provided to predict density and packing fraction, to more completely assess SRO, and to extend consideration of cluster packing schemes to

include fcc, hcp, bcc and simple cubic (sc) symmetries. Four basic model features are derived from the efficient filling of space in extended systems of unequal spheres (Section 2). Additional model features are developed in Section 3 and predictions are provided in Section 4. Atomic size is the primary consideration, but this model relies upon an important chemical contribution. Discussion in Section 5 covers the basic model features, predictive capabilities and implications.

2. The efficient cluster packing model: four basic features

2.1. Efficient cluster packing

Efficiently packed solute-centered clusters with solvent atoms only in the first coordination shell are used in the present model as local RSEs. This employs the primary feature of the stereochemically defined [2] and efficient local atomic packing (ELAP) [3] models. Efficient packing is enabled for the N solvent atoms in the 1st coordination shell when the solute-to-solvent radius ratio R attains specific and predictable values R_N^* [3] (Table 1). Specific configurations for optimally packed isolated hard sphere clusters have been established for these same values of N [48–50], and these are taken here as local RSEs in metallic glass structures. Sub-optimal cluster configurations may also provide relevant local structures [48]. Additional information regarding the rationale and application of efficiently packed solute-centered clusters as local RSEs in metallic glasses is provided elsewhere [3,46–48].

The principle applied here to establish structure beyond the nearest neighbor shell is the efficient filling of space. To accomplish this, efficiently packed solute-centered atomic clusters with solvent atoms only in the 1st coordination shell are imagined to be spheres, and these sphere-like clusters are organized in space to maximize the fraction of space filled. For a dominant cluster-forming solute, these sphere-like clusters all have identical radii, so that an fcc or hcp array provides the most efficient packing of these equal-sized sphere-like clusters. Comparison with a broad range of experimental data (Section 4) shows that many glasses are well-represented by fcc cluster packing, but that simple cubic (sc) cluster packing is also important for

Table 1
Coordination numbers N and corresponding values of R_N^* from [3]

N	R_N^*	N	R_N^*
3	0.155	12 ^a	0.902
4	0.225	13	0.976
5	0.362	14	1.047
6	0.414	15 ^a	1.116
7	0.518	16 ^a	1.183
8 ^a	0.617	17 ^a	1.248
9 ^a	0.710	18 ^a	1.311
10 ^a	0.799	19 ^a	1.373
11	0.884	20 ^a	1.433

^a Clusters typically expected in metallic glasses (Section 3.1).

metal–metalloid glasses. Other periodic, quasi-periodic and aperiodic sphere packings may also be important in the structure of metallic glasses and will be assessed in future studies.

An important consequence of periodic and quasi-periodic cluster packing is that solute atoms occupy ordered sites within the structure, providing a basis for observed MRO. Solute–solute ordering peaks predicted from this model are compared with experimental observations in Section 4 to establish the validity of this concept and to define the cluster packing symmetry. These comparisons show that the present model can be idealized as an fcc or sc array of efficiently packed solute-centered sphere-like clusters. Aperiodic cluster packings may not provide a clear basis for MRO and are not considered further here. It is likely that identifiable solute order extends to no more than a few cluster diameters as a result of atomic relaxations and internal strains. The origin and nature of these internal strains will be described in Section 3.5. It should be clear that solvent–solvent ordering is not a feature of this model. Finally, descriptions of the specific clusters present, of cluster-packing symmetry, and of cluster-sharing modes (vertex, edge, face, see Sections 3.3 and 3.5) are statistical preferences and not a definite specification that must be satisfied everywhere in the structure.

In addition to solvent atoms Ω and the primary cluster-forming solute species α , up to two additional structural sites are produced as a second consequence of this packing scheme. As tetrahedral and octahedral interstices exist in an fcc structure, cluster-tetrahedral and cluster-octahedral sites exist in the efficient cluster packing (ECP) model. These are not interstices, but rather are regions enclosed by efficiently packed α clusters into which the Ω atoms may relax, producing local free volume sufficient to accommodate an additional solute atom. If solutes of the correct sizes (Section 2.4) and chemical interactions (Section 5.3) are available, they can direct the rearrangement of these Ω atoms into more efficiently packed configurations, thus replacing the local free volume with a solute. The sizes of solutes that can be best accommodated in these sites can be different than Ω and α species. Thus, the ECP model is comprised of four topologically distinct atomic constituents including solvent atoms Ω and up to three solutes; an α solute that produces the primary structure-forming clusters, a β solute that occupies cluster-octahedral sites and a γ solute that occupies cluster-tetrahedral sites. sc cluster packing produces only one new inter-cluster solute site so that only two topologically distinct solutes exist in this structure. A final consequence of this cluster packing scheme is that structural defects may occur as a result of solute ordering. This will be discussed in Sections 3.2 and 5.1.

2.2. Overlapping clusters

The second model feature is that nearest-neighbor α clusters overlap in the 1st coordination shell. Ω concentra-

tions in the most stable metallic glasses often range from $\sim 45\%$ to $\sim 60\%$. These values are consistent with overlapping nearest-neighbor α clusters and are inconsistent with non-overlapping clusters. Overlapping clusters also require that each Ω atom will have ~ 2 α atoms as nearest neighbors. Both of these characteristics are well supported by experimental observations (Section 4).

2.3. No cluster orientational order

There is no orientational order amongst clusters in this model so that the majority species (Ω atoms) occupy random positions, consistent with the defining feature of metallic glasses. This feature is also consistent with the requirement that nearest-neighbor α clusters overlap in the 1st coordination shell, since cluster symmetries [48] and cluster packing symmetries are generally incommensurate. This model feature provides an important distinction from the icosahedral glass model proposed for quasi-crystalline structures, where all icosahedra share the same spatial orientation [51].

2.4. Solute atom sizes

The relative atomic sizes that produce ELAP in solute-centered clusters (Table 1) are strongly preferred for all solutes in metallic glasses [3]. Thus, it is a fundamental feature of this model that α , β and γ solutes all prefer sizes R^* relative to Ω atoms. As a consequence, α , β and γ atoms all form efficiently packed solute-centered clusters with Ω atoms only in the first coordination shell. Along with α , the β and γ clusters form ordered arrays within the structure, and they overlap with α clusters in the first shell. β and γ clusters generally share faces with α clusters, but internal strains may introduce some degree of edge- and vertex-sharing (Section 3). The ECP structure is thus comprised of interpenetrating arrays of efficiently packed solute-centered clusters. Two-dimensional representations showing these basic model features are given in Fig. 1.

Chemically distinct elements possessing R values within $\pm 2\%$ of one another are considered to be topologically equivalent. Thus, a Zr–Al–(Cu,Ni) metallic glass is a ternary alloy from a structural viewpoint since $R_{\text{Ni}} \cong R_{\text{Cu}}$. These two elements are expected to occupy the same sites within the structure. The atomic radii used in the present model are shown in Table 2 and a discussion of the basis and errors associated with these values is given in Section 5.4.

3. The efficient cluster packing model: detailed features

3.1. Nomenclature and convention

Metallic glass structures can be specified by combinations of 1, 2 or 3 topologically distinct solutes. This introduces significant diversity in the number of possible structures (Section 5.1.4), and so a structure-specific

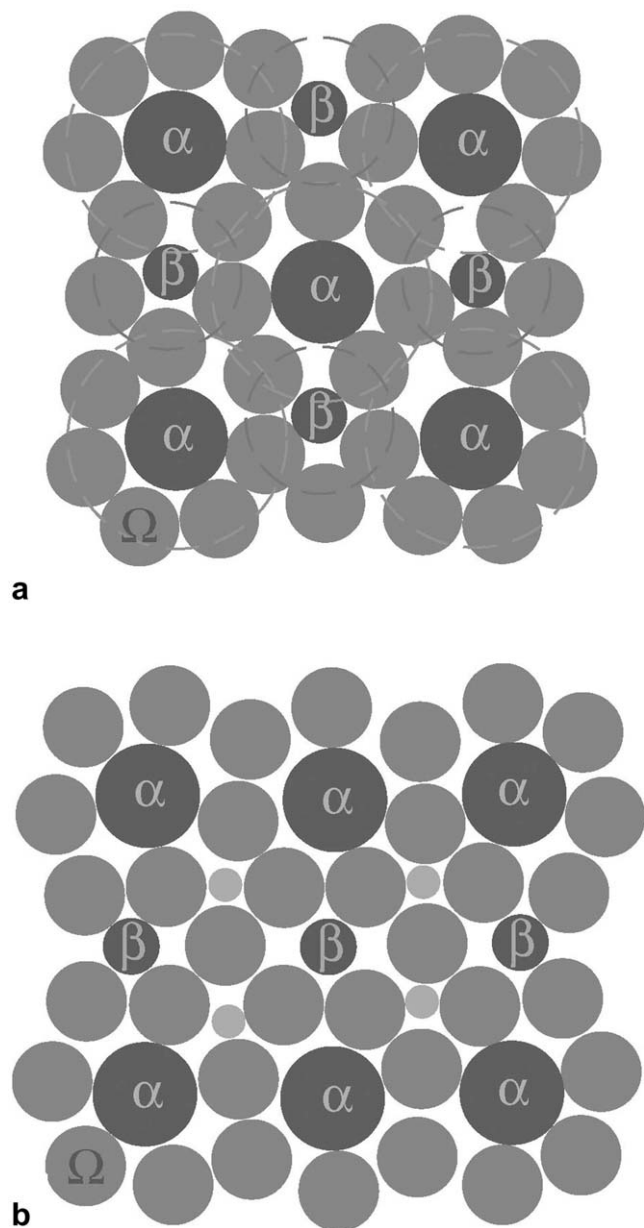


Fig. 1. 2-dimensional representations of an efficient cluster packing structure in (a) the {100} plane and (b) the {110} plane of a single fcc cluster unit cell. The features of interpenetrating solute-centered clusters, efficient atomic packing around each solute, ordering of solute atoms and randomness of solvent atoms are illustrated in these schematic figures. The dashed circles in (a) show overlapping α and β clusters. The four small γ solutes are not labelled in (b) for clarity. α , β and γ solutes have 7, 5 and 4 nearest-neighbour Ω atoms, respectively.

nomenclature is required. Consider a system where α solutes occupy positions of an fcc cluster lattice and have $R_\alpha \cong 0.902$ so that $N_\alpha = 12$ (Table 1). Further, β and γ sites are filled by solutes with $R_\beta \cong 0.799$ and $R_\gamma \cong 0.710$ to produce efficiently packed clusters with $N_\beta = 10$ and $N_\gamma = 9$. Ω atoms occupy random positions as a result of the basic model features. Finally, all sites are filled by their respective species. This structure is designated as $\langle 12,10,9 \rangle_{\text{fcc}}$ representing the putative coordination numbers of α , β and γ

Table 2
Atomic radii for metallic glass structures

Element	At #	Radius (pm)	Element	At #	Radius (pm)	Element	At #	Radius (pm)
C	6	77	Ga	31	132	Mg	12	160
B	5	78	V	23	134	Sc	21	164
P	15	100	Zn	30	138	Nd	60	164
Si	14	102	Mo	42	139	Hf	72	167
Be	4	112	Pd	46	141	Gd	64	174
Ge	32	114	W	74	141	Er	68	176
Cu	29	127	Ag	47	142	Dy	66	177
Fe	26	128	Al	13	143	La	57	187
Co	27	128	Ti	22	146	Y	39	180
Ni	28	128	Nb	41	146	Sm	62	181
Cr	24	130	Ta	73	149	Ce	58	182
Mn	25	132	Zr	40	158	Ca	20	197

solutes, respectively. A portion of this structure is shown in Fig. 2. By convention, the largest N represents α solutes, and β and γ solutes are progressively smaller. A glass structure is thus specified by one to three integers that decrease in magnitude, representing the putative solute coordination numbers. The cluster packing symmetry can be indicated with a subscript when this is important.

The relative solute sizes typically found in metallic glasses suggest that $8 \leq N \leq 20$. Clusters with $N = 11$ and $N = 12$ have solutes that are topologically nearly identical, and so it is proposed that clusters with $N = 11$ will not be observed in favor of more efficiently packed icosahedra. Further, clusters with $N = 13$ and $N = 14$ are not common [3], so that 10 values of R^* and N are generally observed in metallic glasses (Table 1).



Fig. 2. A portion of a $\langle 12,10,9 \rangle_{\text{fcc}}$ cluster unit cell representing Zr–(Al,Ti)–(Cu,Ni)–Be alloys [47]. α sites are occupied by blue spheres, β sites are occupied by purple spheres and γ sites are occupied by orange spheres. Pink Zr solvent spheres form icosahedra around each α solute. There is no orientational order amongst the icosahedral clusters. The α and four of the β atoms occupy roughly the same plane, and γ solutes are in a parallel plane displaced by $\sim(1/4)$ of the cluster unit cell length Λ_0 . A fifth β solute occupies the center of the cluster unit cell.

The convention adopted here for a chemical description of metallic glasses lists Ω first, followed by solutes in order of decreasing size. Elements with R within $\pm 2\%$ of each other are considered to be topologically equivalent and are enclosed in parentheses. Concentrations are given in atomic percent and are indicated as a subscript following the respective atomic species.

3.2. Defects

Since specific sites and occupancies are identified in the ECP model, point defects can exist. From comparisons between predicted and actual features (Section 4) and logical arguments (Section 5), it is concluded that ‘vacancy’ and solute anti-site defects are common on β and γ sites. Since β and γ sites are not atomic interstitials, an unoccupied β or γ site is not a vacancy, but is rather an inter-cluster region of relatively inefficiently packed Ω atoms that has sufficient free volume to accept a solute atom. For convenience, the term ‘vacancy’ will be used here with this understanding. Actual atomic vacancies, in the sense of a localized unoccupied volume sufficient to accept an atom, are not expected to occur in metallic glasses [52,91]. Experimental evidence suggests that anti-site defects on Ω sites are relatively common (Section 4.2), providing limited solute–solute nearest neighbor associations. Although anti-site defects on α sites may exist, they are generally not necessary to achieve quantitative agreement with experimental measurements and so are not suggested to be common. Kroger–Vink notation is used for point defects, so that an α anti-site solute on a β site is denoted as α_β , and an unoccupied γ site is shown as V_γ . A more complete discussion is given of point defects (Section 5.1.3) and structural diversity (Section 5.1.4).

3.3. Medium range atomic packing and the cluster unit cell length

Cluster packing provides a framework for calculating the cluster unit cell vector lengths A_{hkl} (Fig. 3), and ultimately for determining the cluster unit cell length A_0 . A_{hkl} values can be determined from atomic radii r and from specification of whether adjacent clusters share common faces, edges or vertices. The most efficient packing is obtained when adjacent clusters share a common face, and this is commonly observed for adjacent unlike clusters (Section 4). Since an equilateral trigonal arrangement of Ω atoms provides the most efficient packing in the 1st coordination shell, nearest-neighbor solutes for adjacent face-sharing clusters will typically occupy opposite caps of a trigonal bipyramid. The solute–solute separation for this configuration is obtained from geometry. Similar geometric arguments allow determination of solute–solute separations for edge- and vertex-sharing clusters. These relationships are given in Appendix A.

The cluster unit cell length A_0 for fcc packing of α clusters is obtained from A_{100} , $(A_{110}/\sqrt{2})$ and $(A_{111}/\sqrt{3})$, and

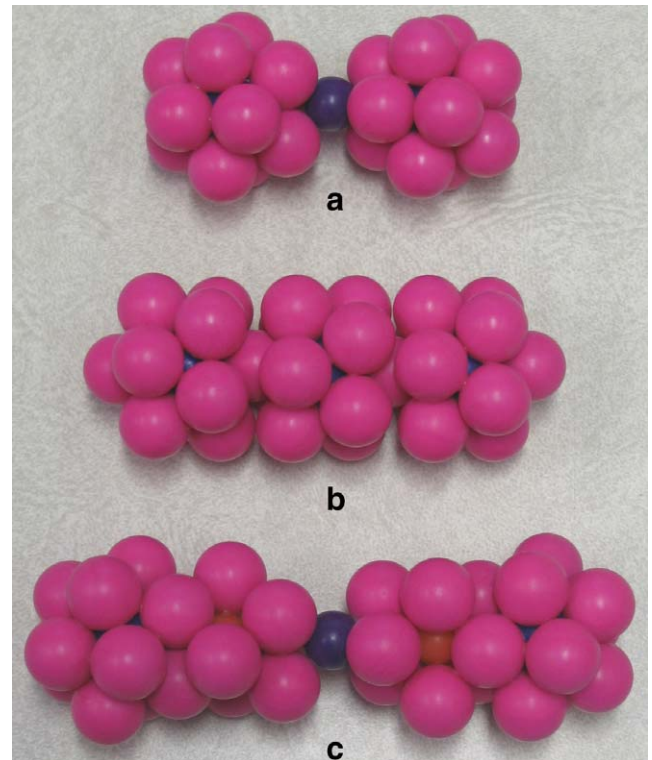


Fig. 3. Cluster packing along (a) $\langle 100 \rangle$, (b) $\langle 110 \rangle$ and (c) $\langle 111 \rangle$ unit directions of the $\langle 12,10,9 \rangle_{\text{fcc}}$ structure (Section 3.1). Ω atoms are pink, α solutes are blue, β solutes are purple and γ solutes are orange. Adjacent unlike clusters share faces in (a) and (c), and vertex sharing between nearest-neighbor α clusters is shown in (b). The α clusters are icosahedra and γ clusters are distorted tri-capped trigonal prisms. The β clusters in (a) and (c) have six nearest-neighbor Ω atoms shown, and the remaining four required for $N = 10$ have been removed for clarity.

is given as reduced unit cell lengths (A_0 normalized by r_Ω) in Table A1. Different A_0 values are obtained from each unit direction and for face-, edge- or vertex-sharing. The largest A_0 for the most efficiently packed (i.e., face-sharing) configuration controls the size of A_0 , and internal tensile strains exist along other directions. Determination of A_0 in structures that contain anti-site occupancy on β or γ sites is discussed and relations for structures with vacancies on β and on $(\beta + \gamma)$ sites are provided in Appendix A with results listed in Tables A2 and A3. Similar equations are provided in Appendix A for sc cluster packing.

3.4. A representative structural element at the medium-range length scale

Even though internal strains eliminate long range solute order, it is nevertheless useful to consider a limited volume of regularly positioned clusters. This enables use of crystallographic concepts to describe atomic structure as in the previous subsection. Further, this provides a basis to define an RSE at the medium range length scale. Values of A_0 in metallic glasses generally range from ~ 0.4 – 1.1 nm (Table 6). These A_0 values are roughly equivalent to the extent of MRO in metallic glasses, and so it is suggested

that a single cluster unit cell provides a meaningful RSE at a medium-range length scale. The relevance of this assignment is explored in Section 4.2. Part of a $\langle 12,10,9 \rangle_{\text{fcc}}$ medium range RSE is shown in Fig. 2.

3.5. Origin and nature of internal strains

In general, different A_0 values are derived from packing along different unit directions. A_0 values derived from face-sharing clusters along $\langle 111 \rangle$, $\langle 110 \rangle$ and $\langle 100 \rangle$ in Table A1 are $6.251(r_\Omega)$, $4.276(r_\Omega)$ and $5.782(r_\Omega)$, respectively. A_0 is given by the largest of these values, and tensile strains exist along $\langle 100 \rangle$ and $\langle 110 \rangle$. These strains are reduced when clusters adopt edge- or vertex-sharing configurations. For example, A_0 derived for edge-sharing clusters along $\langle 100 \rangle$ is $6.227(r_\Omega)$, which is very close to A_0 obtained from face-sharing clusters along $\langle 111 \rangle$. Edge-sharing clusters may therefore be common along $\langle 100 \rangle$ to reduce internal strains. A tensile strain remains along $\langle 110 \rangle$ even when clusters adopt vertex-sharing arrangements, so that nearest neighbor α clusters are expected to share vertices for this structure. A large number of possible structures have been assessed, including many of the structures discussed in Section 5.1.4. Further, structures with fcc, bcc and sc cluster packing have been considered. The preference for vertex-sharing between nearest-neighbor α clusters, for edge-sharing between α and β clusters and for face-sharing between α and γ clusters is a general result for most structures with fcc cluster packing. In structures with sc cluster packing, nearest-neighbor α clusters typically share edges while common faces are shared between α and β clusters.

4. Model validation

The ECP model provides flexibility sufficient to reproduce nearly any composition, and so it is not instructive to do so as a validation. However, compositional trends in metallic glasses can be reasonably reproduced using only two major features of the ECP model – distinct relationships between the number of Ω , α , β and γ sites derived from ordered cluster packing, and structural defects on β and γ sites. Model validation via composition calculations (Section 4.1) uses only these features to underscore their importance and robustness. The full range of structural defects is used to calculate compositions for MRO (Section 4.2), SRO (Section 4.3), and density (Section 4.4), since matching compositions is not the purpose of these sections and accurate compositions are required to fit these structure-specific features. While comparison with diffraction data generally suffers from non-uniqueness, the present model provides a sensitive check via solute–solute ordering. Predictions are considered for fcc, hcp, bcc and sc cluster packing. Additional validations include efficient atomic packing and the number of topologically distinct solutes (Section 4.5).

4.1. Metallic glass constitution

The approach for calculating atomic concentrations from the ECP model is outlined in Section 4.1.1 and is applied to a broad range of metallic glasses. Comparisons between predicted and actual topologies (Section 4.1.2) are illustrated with atomic size distribution profiles (ASDPs) in Figs. 4–8. A glass constitution is shown by a series of points in these figures, where each point represents the atomic concentration and size relative to the solvent of each topologically distinct species in that glass. Filled symbols are actual glass compositions and open symbols give the present predictions. Topologically equivalent atoms occupy the same structural sites, and so their concentrations are summed and an average value of R is used. Vertical gray bands illustrate a range of $\pm 2\%$ relative to the ideal radius ratios R^* . A detailed description of this method for illustrating metallic glass topology is given in [33].

4.1.1. Composition calculation methodology

To determine composition, the number of sites and the occupancy of those sites must be specified. The cluster packing model allows the total number of j sites per α site \hat{S}_j to be specified. For fcc packing, there is 1 β site and 2 γ sites for each α site, so that $\hat{S}_\beta = 1$ and $\hat{S}_\gamma = 2$. For sc and bcc cluster packing $\hat{S}_\beta = 1$ and $\hat{S}_\beta = 1.5$, respectively. γ sites do not exist in sc and bcc cluster packing structures, so that $\hat{S}_\gamma = 0$. α clusters share common vertices, so that the number of Ω atoms in the 1st shell of an α cluster $N_{\alpha-\Omega}$ are shared between that cluster and ϕ overlapping nearest-neighbor α clusters. The total number of Ω sites per α site is thus

$$\hat{S}_\Omega = [N_{\alpha-\Omega} / (1 + (\phi / N_{\alpha-\Omega}))] \quad (1)$$

where $N_{\alpha-\Omega}$ is specified by R^* [3]. All Ω atoms are associated with α clusters in this approach, and so additional Ω

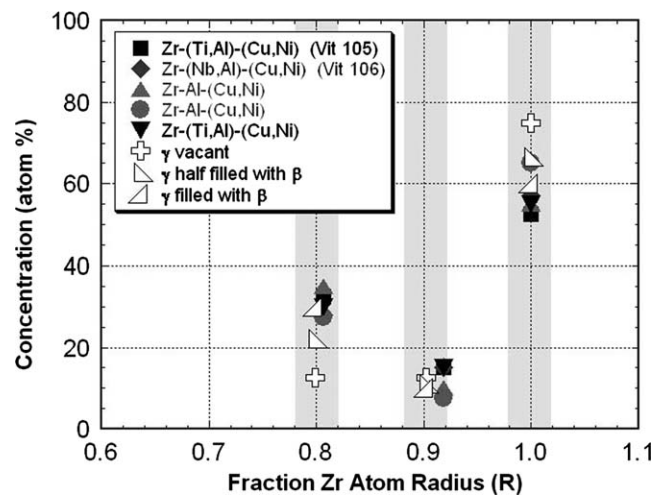


Fig. 4. Comparison of relative atomic sizes and concentrations with predictions from the efficient cluster packing model for selected Zr-based glasses without Be representing $\langle 12,10 \rangle$ structures. Glass compositions are taken from [67,89,90].

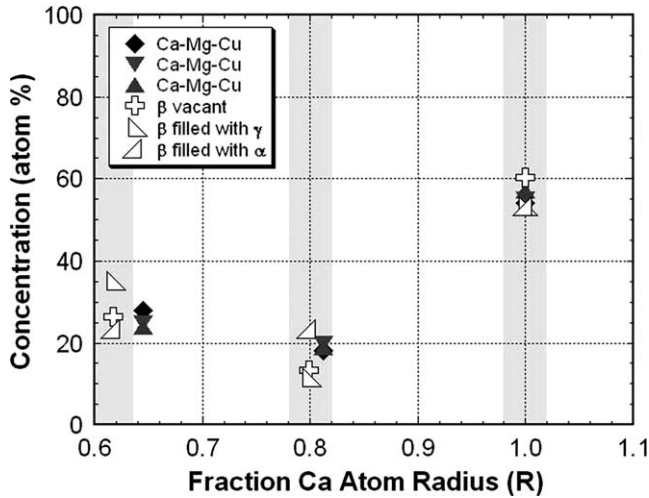


Fig. 5. Comparison of actual and predicted relative atomic sizes and concentrations for selected Ca-based BMGs representing $\langle 10,8 \rangle$ glasses. Glass compositions are taken from [55].

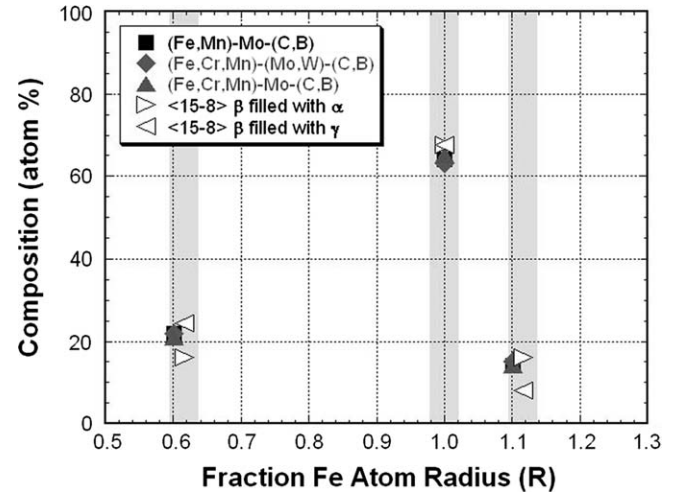
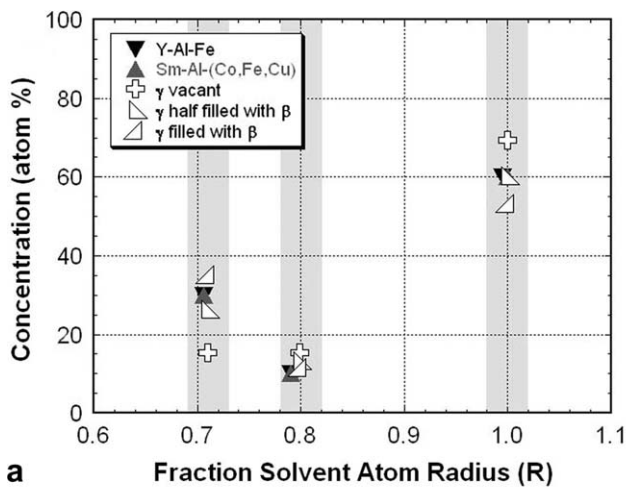
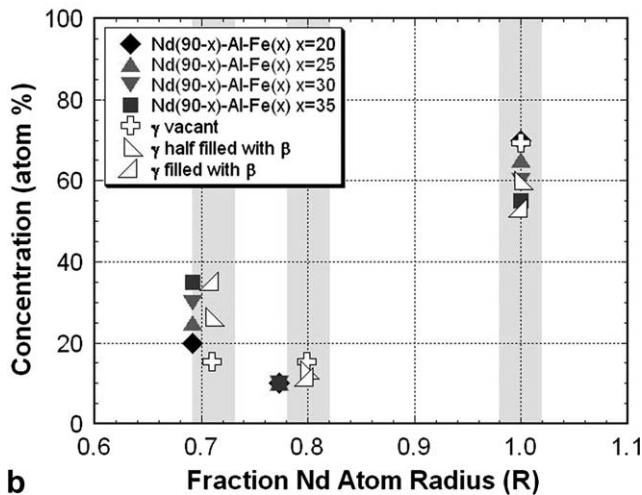


Fig. 7. Comparison of actual and predicted relative atomic sizes and concentrations for selected Fe-based glasses representing the $\langle 15,8 \rangle$ structure. Glass compositions are taken from [69,70].



a



b

Fig. 6. Comparison of actual and predicted relative atomic sizes and concentrations for selected rare earth metal-based BMGs. (a) Y- and Sm-based BMGs representing $\langle 10,9 \rangle$ glasses and (b) Nd-based BMGs representing $\langle 10,9 \rangle$ glasses. Glass compositions are taken from [59,60].

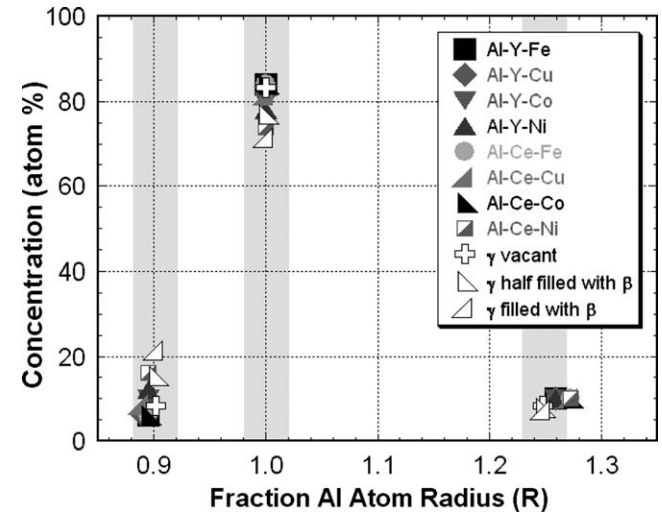


Fig. 8. Comparison of actual and predicted relative atomic sizes and concentrations for selected Al-(RE)-(early transition metal) glasses representing the $\langle 17,12 \rangle$ structure. Similar profiles and agreement exist for Al-(late transition metal)-(early transition metal) glasses represented by the $\langle 15,12 \rangle$ and $\langle 16,12 \rangle$ structures and Al-(RE)-(early transition metal) glasses represented by the $\langle 18,12 \rangle$ structure. Glass compositions are taken from [71].

sites are not produced by addition of β or γ solutes. The total number of structural sites is $\sum S = \sum_j \bar{S}_j$. The site occupancy $S(i_j)$ is the number of species i that occupy j sites per α site (Table 3). The total number of species i per α site is obtained by summing over all j sites, $\bar{S}_i = \sum_j S(i_j)$. The species total is $\sum S = \sum_i \bar{S}_i = \sum_{i,j} S(i_j)$, which matches the total number of structural sites.

With this as a background, the concentration in atomic percent of species i is given by

$$C_i = 100\bar{S}_i / \sum S \quad (2)$$

The composition of a metallic glass structure can thus be determined for any set of $S(i_j)$ values. For example, α , β ,

Table 3
Structural sites and site occupancies per α site

		Species (i)					Site sum
		Ω	α	β	γ	V	
Site (j)	Ω	$S(\Omega_\Omega)$	$S(\alpha_\Omega)$	$S(\beta_\Omega)$	$S(\gamma_\Omega)$	$S(V_\Omega)$	\widehat{S}_Ω
	α	$S(\Omega_\alpha)$	$S(\alpha_\alpha)$	$S(\beta_\alpha)$	$S(\gamma_\alpha)$	$S(V_\alpha)$	\widehat{S}_α
	β	$S(\Omega_\beta)$	$S(\alpha_\beta)$	$S(\beta_\beta)$	$S(\gamma_\beta)$	$S(V_\beta)$	\widehat{S}_β
	γ	$S(\Omega_\gamma)$	$S(\alpha_\gamma)$	$S(\beta_\gamma)$	$S(\gamma_\gamma)$	$S(V_\gamma)$	\widehat{S}_γ
Species sum		\overline{S}_Ω	\overline{S}_α	\overline{S}_β	\overline{S}_γ	\overline{S}_V	$\sum S$

γ and Ω sites are fully occupied by these respective species in the $\langle 12,10,9 \rangle$ idealized structure (Section 3.1), so there are no defects and $S(i_j) = 0$ for $i \neq j$. Site occupancies are $\overline{S}_\alpha = S(\alpha_\alpha) = \overline{S}_\beta = S(\beta_\beta) = 1$, $\overline{S}_\gamma = S(\gamma_\gamma) = 2$ and $\overline{S}_\Omega = S(\Omega_\Omega) = 6$ from Eq. (1), since $\phi = N_{\alpha-\Omega} = 12$. The concentrations are thus $C_\alpha = 10\%$, $C_\beta = 10\%$, $C_\gamma = 20\%$ and $C_\Omega = 60\%$.

A vast number of binary and ternary metallic glasses exist, some of which are sufficiently stable to be considered bulk metallic glasses. Further, many glasses exist with >4 chemically distinct species. Thus, a reasonable account of defects is necessary. A simple view is that α and Ω sites are completely filled by their respective species while β and γ sites can be occupied by their respective solutes, by solute anti-site defects or by ‘vacancies’. β and γ sites can be progressively filled by solutes, providing a range in compositions. A mixture of solute species on a given solute site is not considered. Although this simplified model considers less than 40% of the defects available, compositions calculated in this way are able to represent the major features of composition profiles for a full range of metallic glass systems (Section 4.1.2).

More rigorous account of defects is necessary for quantitative predictions of MRO, partial coordination numbers and density. Additional defects considered in these comparisons include solute anti-site defects on α and Ω sites and Ω anti-site defects on α sites. Vacancies on α or Ω sites and solvent anti-site defects on β and γ sites are not required to achieve reasonable agreement with experimental data. Site occupancies needed to match experimental compositions exactly and their influence on MRO (Section 4.2), partial coordination numbers (Section 4.3) and density (Section 4.4) will be provided in these respective sections.

4.1.2. Comparison with metallic glass compositions

The Zr–Ti–(Cu,Ni)–Be family of Vitreloy alloys is represented by the $\langle 12,10,9 \rangle$ structure, and the predicted atomic concentrations are $C_\Omega = 60\%$, $C_\alpha = 10\%$, $C_\beta = 10\%$ and $C_\gamma = 20\%$. Reasonable agreement is achieved for some of the most stable Zr glasses that represent this class of structures [47]. Zr BMGs without Be are represented by the $\langle 12,10 \rangle$ structure with defects on γ sites. A range of compositions is calculated in Fig. 4 as γ sites are progressively filled with solutes that most closely fit in these sites – β solutes. Very good agreement is shown, especially for the model where β_γ anti-site defects completely fill γ sites.

A new family of Ca BMGs has recently been reported [53–58], and appropriate structural models include $\langle 10,9,8 \rangle$ for Ca–Mg–Zn–Cu and Ca–Mg–(Al,Ag)–Cu, $\langle 10,9 \rangle$ for Ca–Mg–Zn and $\langle 10,8 \rangle$ for Ca–Mg–Cu. The large solvent enables structures with relatively smaller solutes, so that $N_{\alpha-\Omega}$ and \widehat{S}_Ω are different than for Zr glasses. The compositions for a $\langle 10,9,8 \rangle$ structure are $C_\alpha = 11.7\%$, $C_\beta = 11.7\%$, $C_\gamma = 23.4\%$ and $C_\Omega = 53.2\%$. An intervening unoccupied coordination state (Section 5.1.4) exists in the $\langle 10,8 \rangle$ system, and it is assumed that Mg occupies α sites, Cu occupies γ sites and all β sites are vacant, so that β sites can be filled by either α or γ solutes. Additional discussion of possible defect states for topological ternary glasses with an intervening unoccupied coordination state is given in Section 5.1.4. Good agreement between predicted and actual topologies is obtained for $\langle 10,8 \rangle$ (Fig. 5), $\langle 10,9 \rangle$ and $\langle 10,9,8 \rangle$ [47] Ca BMGs.

Rare earth (RE) elements form BMGs with the $\langle 10,9 \rangle$ structure including Y–Al–(Cu,Fe,Co) [59], Sm–Al–(Cu,Fe,Co) [59], Nd–Al–Fe [60] and La–Al–(Cu,Ni,Co) [61]. Agreement between actual and predicted topologies is good for Y- and Sm-based glasses especially when γ sites are either half filled or completely filled with β solutes (Fig. 6a). The best fit for La–Al–Ni BMGs is obtained when all γ sites are vacant. Nd–Al–Fe BMGs are stable over a significant concentration range of Fe [60], and this is very well predicted by the concentration range produced as V_γ are progressively filled by β_γ (Fig. 6b). Y–Sc–Al–(Co,Ni) BMGs [62] are based on the $\langle 10,9 \rangle$ Y glasses described above. Sc was added to occupy the $\langle 12 \rangle$ coordination state as prescribed by $R^* = 0.902$ from [3], thus producing a $\langle 12,10,9 \rangle$ structure. The relative atomic sizes of the constituents in this system match very closely values of R^* [3], but the concentrations provide only a nominal match using the simplified assumptions.

In the glasses discussed thus far, all solutes have been smaller than Ω atoms. However, many glasses possess solutes that are larger than Ω atoms. Mg–(RE)–(Ni,Cu) glasses with $\langle 15,10 \rangle$ structures are stable over a range of concentrations [63], and (Cu,Ni) contents as low as 3% still produce a fully amorphous structure [64]. Predicted concentrations show good agreement with observed constitution and with the concentration range for the smallest solute species for the $\langle 15,10 \rangle$ structure. The most stable Mg–(RE)–(Cu,Ni) glasses are obtained for 25% Cu [65], consistent with a predicted concentration of 24.3% for a $\langle 15,10 \rangle$ structure where all β and γ sites are filled by β solutes.

Pd glasses [66,67] have a $\langle 12,9 \rangle$ structural representation. The solutes skip a coordination state, and computed concentrations represent cases where V_β are filled either by γ or α solutes. While a good match is obtained for earlier Pd-based glasses, a poorer fit results for the best Pd glasses, which often contain equal concentrations of Ω and α (Cu,Ni) species. Like the Nb–Ni system, Pd–(Ni,Cu)–P glasses display an unusually broad range of compositions where the Pd solvent becomes a minority species and

(Cu,Ni) become the solvent [66]. These concentrations can only be rationalized by a significant concentration of α_Ω defects (see Section 4.2 for analysis of the concentration of α_Ω defects). In support of this idea, diffraction evidence suggests that Cu may substitute for Pd [68].

Fe-based glasses represent some of the most complex metallic glasses, containing as many as seven chemically distinct atomic species with radii that span a range from 77 to 180 pm. Metallic glasses with exceptionally low magnetic susceptibility are produced with the $\langle 10,8 \rangle$ structure in MetGlas[®] alloys and with the $\langle 15,10,8 \rangle$ structure for FINEMET[®] alloys. Fe-BMGs have recently been discovered with $\langle 15,8 \rangle$, $\langle 17,15,8 \rangle$ and $\langle 19,15,8 \rangle$ structures [69,70]. Agreement between predicted and actual topologies is very good for all of these glasses (Fig. 7 and [47]).

Four distinct ternary Al glasses of $\langle 15,12 \rangle$, $\langle 16,12 \rangle$, $\langle 17,12 \rangle$ and $\langle 18,12 \rangle$ are commonly reported. The α solutes are either late transition metal (Zr, Hf) or RE (Y, Ce, Gd, La, Er, etc.) elements and the transition metal (TM) elements Cu, Ni, Fe and Co are β solutes. Very good agreement between calculated and observed topologies is shown for all four structural classifications (see Fig. 8 for $\langle 17,12 \rangle$ glasses). Binary glasses are also sometimes formed from these structures by omitting the β solutes [71].

Vacancy or anti-site defects exist on β and γ sites in binary glasses, and a high solute concentration can be produced when α atoms fill both β and γ sites. Such a structure is suggested in binary glasses that span the equi-atomic composition, including Zr–Cu, Zr–Ni and Nb–Ni. Stable glasses are produced in a narrow composition range in other systems, including the family of metal–metalloid glasses, where the optimum metalloid concentration is typically 18–20%. This is in reasonable agreement with predicted concentrations for structures with β vacancies that range from 17.9% for an $\langle 8 \rangle_{sc}$ glass to 13.8% for a $\langle 10 \rangle_{sc}$ glass (sc cluster packing is assumed for glasses with $N_{\alpha-\Omega} \leq 10$ based on analysis below). Good agreement is obtained for a number of binary metallic glasses that span a range of relative solute sizes [47].

4.2. Medium range atomic order

Although solute–solvent and solvent–solvent MRO is not a feature of the ECP model, solute–solute ordering is provided. Comparison between experimental solute–solute partial radial distribution functions (p-RDFs) and ECP model predictions allows validation of the presence and type of cluster-packing symmetry, since different cluster packing symmetries give clearly distinct solute–solute distributions. Diffraction also provides a basis for evaluating the defect state. A solute–solute nearest-neighbor peak is often observed in metallic glasses, providing clear evidence for i_Ω defects. The intensity of the $\alpha-i$ solute–solute diffraction peak depends on the multiplicity $M_{\alpha-i}$, which depends on the concentration of solute anti-site defects $S(i_\Omega)$ through the relationship

$$M_{\alpha-i}^{fcc} = 2\phi \cdot S(i_\Omega)[S(i_\alpha) + S(i_\beta) + S(i_\gamma)]/\hat{S}_\Omega \quad (3a)$$

The same equation holds for bcc cluster packing, where $S(i_\gamma) = 0$. For sc cluster packing,

$$M_{\alpha-i}^{sc} = 2\phi \cdot S(i_\Omega)[S(i_\alpha) + 2S(i_\beta)]/\hat{S}_\Omega \quad (3b)$$

p-RDF diffraction data provides additional information regarding defects. fcc packing of α clusters will produce α – α p-RDFs consistent with fcc symmetry in binary glasses with vacant β and γ sites ($V_\beta + V_\gamma$). However, for fcc packing of α clusters filling of inter-cluster sites produces sc symmetry of α solutes when the $(\alpha_\beta + V_\gamma)$ defect state dominates, and bcc solute symmetry is produced when $(\alpha_\beta + \alpha_\gamma)$ anti-site defects exist on all β and γ sites.

Although a large amount of diffraction data are available, there is relatively little high quality data for solute–solute p-RDFs, as many studies emphasize solute–solvent distributions. Predictions from the ECP model are compared with experimental solute–solute p-RDFs for $Ni_{63}Nb_{37}$ [72], $Nb_{60}Ni_{40}$ [72], $Ti_{60}Ni_{40}$ [73], $Zr_{65}Ni_{35}$ [74] and $Ni_{81}B_{19}$ [4]. In these binary glasses, $S(\beta_j) = S(\gamma_j) = 0$, greatly simplifying specification of the defect concentrations. When present, a solute–solute nearest neighbor ordering peak was used to determine $S(\alpha_\Omega)$ from Eq. (3), which in turn was used to calculate $S(\Omega_\Omega)$ from Eq. (1) since $S(\Omega_\Omega) = \hat{S}_\Omega - S(\alpha_\Omega)$ for binary glasses. $S(\Omega_\alpha)$ was assumed to be zero, and C_α was finally matched by sequentially filling α , β and γ sites. The same defect state used to predict MRO via A_0 and p-RDFs here was also used to calculate partial coordination numbers and density later in this manuscript. Atomic radii were taken from the diffraction studies cited. Predicted solute–solute p-RDFs are obtained from an unrelaxed cluster unit cell and do not account for internal strains. The mean atomic density $\bar{\rho}$ was varied to fit the height of first major ordering peak and predicted intensities are normalized by a term $M/4\pi x^2 \bar{\rho}$ to account for radial distance x .

$Ni_{63}Nb_{37}$ is represented as a $\langle 16 \rangle_{fcc}$ glass with Nb solutes fully occupying α , β and γ sites ($\alpha_\beta + \alpha_\gamma$) defect state. The composition is matched exactly for $S(\alpha_j)$ values given in Table 4. A A_0 of 1.097 nm is calculated, and the predicted Nb–Nb peaks are shown in Fig. 9a. A good fit to experimental peak positions is shown, including presence of the Nb–Nb nearest neighbor peak and a faithful reproduction of the splitting of the first ordering peak. The predicted height of the solute–solute nearest neighbor peak is significantly higher than experiment, but a match is achieved for a small change in alloy composition (to $Ni_{67}Nb_{33}$) so that this prediction is rather sensitive to the actual alloy composition. Other defects, such as di-solute centered clusters [75] may exist and would decrease the disparity between these two values.

A similar comparison is shown in Fig. 9b for $Nb_{60}Ni_{40}$. This is a $\langle 12 \rangle_{fcc}$ glass with $(\alpha_\beta + \alpha_\gamma)$ anti-site defects, although γ sites are only partially filled by α solutes. The predicted concentration is $Nb_{60}Ni_{40}$ and A_0 is 0.985 nm using $S(\alpha_j)$ values in Table 4. A solute–solute nearest

Table 4
 $S(i_j)$ values used to predict MRO, partial coordination numbers and density

Glass	r_Ω (pm)	r_α (pm)	$S(\alpha_\Omega)$	$S(\alpha_\alpha)$	$S(\alpha_\beta)$	$S(\alpha_\gamma)$	Ref.
Ni ₈₁ B ₁₉ (9) _{sc}	126	85	0 ^{a,b}	1	0.192	NA	[4]
Ni ₆₄ B ₃₆ (9) _{sc}	127.5	86	0.548 ^c	1	1	NA	[84]
Fe ₈₀ B ₂₀ (9) _{sc}	128.5	85.5	0 ^{a,b}	1	0.249	NA	[85]
Ni ₈₀ P ₂₀ (10) _{sc}	124	100	0 ^{a,b}	1	0.581	NA	[76]
Zr ₆₅ Ni ₃₅ (10) _{sc}	157.5	133	1.593 ^a	1	0.161	NA	[74]
Nb ₆₀ Ni ₄₀ (12) _{fcc}	149	125	0.639 ^a	1	1	0.185	[72]
Ni ₆₃ Nb ₃₇ (16) _{fcc}	125	153	1.053 ^c	1	1	2.00	[72]
Al ₉₀ Y ₁₀ (17) _{fcc}	180	143	0.110 ^c	1	0	0	[86]

^a Calculated using the height of the experimental α - α nearest-neighbor peak.

^b Calculated from the experimental value of $N_{\alpha-\alpha}$.

^c Calculated to match composition.

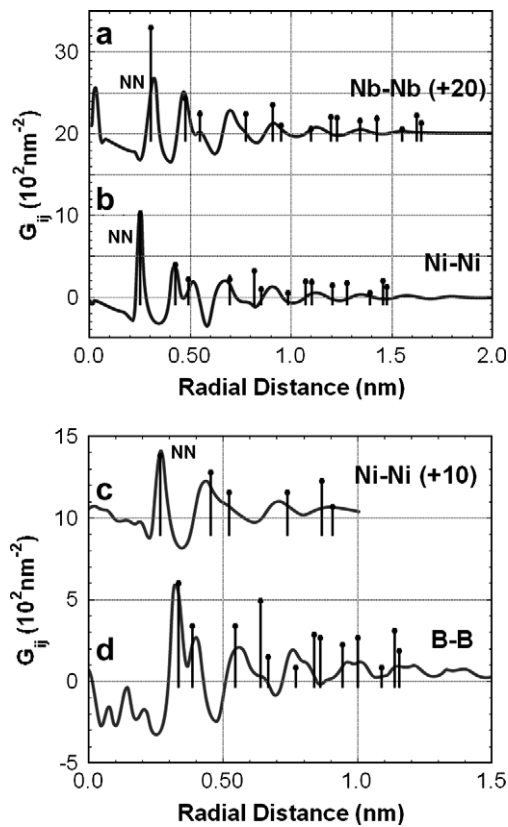


Fig. 9. Comparison of predicted and experimental solute-solute radial distribution functions for (a) Nb–Nb separations in Ni₆₃Nb₃₇, (b) Ni–Ni separations in Nb₆₀Ni₄₀, (c) Ni–Ni separations in Zr₆₅Ni₃₅ and (d) B–B separations in Ni₈₁B₁₉. *fcc* cluster packing is modelled in (a and b), and *sc* cluster packing is modelled in (c and d). A good fit is seen to a length scale of 0.7–1.3 nm. The curves representing experimental data have been redrawn from [4,17,74].

neighbor peak shows the presence of α_Ω anti-site defects, and the same value of $S(\alpha_\Omega)$ gives good agreement with both composition and diffraction data. Ti₆₀Ni₄₀ gives results similar to Nb₆₀Ni₄₀, since $r_{Ti} \approx r_{Nb}$ and the Ni–Ni p-RDFs for these two glasses are very similar.

Zr₆₅Ni₃₅ is a (10) glass. A single set of $S(i_j)$ values does not give simultaneous agreement with composition and sol-

ute-solute MRO peaks for *fcc*, *hcp* or *bcc* cluster packing. However, *sc* cluster packing gives good agreement for both of these features (Fig. 9c) with $S(\alpha_j)$ values given in Table 4. Thus, Zr₆₅Ni₃₅ is a (10)_{sc} structure with (α_β) defects. A high concentration of α_Ω defects simultaneously fits the composition and the measured Ni–Ni nearest neighbor peak.

Atomic radii and coordination numbers [4] suggest a (9) structure for Ni₈₁B₁₉. Acceptable agreement with both composition and MRO cannot be achieved for *fcc*, *hcp* or *bcc* cluster packing. However, a (9)_{sc} structure with (α_β) defects matches the concentration with $S(\alpha_j)$ values given in Table 4 and gives modest agreement with experimental p-RDF peaks using the predicted A_0 of 0.362 nm. Better agreement with measured MRO is achieved using a slightly larger value of 0.385 nm (Fig. 9d), which is achieved by edge-sharing of adjacent α clusters. There are no B–B nearest neighbors in Ni₈₁B₁₉ [4], consistent with the value of $S(\alpha_\Omega)$ used here.

Reasonable agreement is also achieved for the (10)_{sc} structure with α_β defects in Ni₈₀P₂₀ [76]. The basic features of the experimental P–P p-RDF are reproduced, including absence of a P–P nearest neighbor peak and splitting of the first ordering peak. As with Ni₈₁B₁₉, a small expansion (~8%) of A_0 to 0.430 nm is required to fit p-RDF data well. Ni–B and Ni–P glasses share an unusually strong metalloid–metalloid avoidance which is manifested as $S(\alpha_\Omega) = 0$ and which may also be responsible for this small expansion in cluster separation.

4.3. Partial coordination numbers

The following analysis provides an approach to calculate the four partial coordination numbers in binary glasses when both species may occupy the 1st coordination shell.

4.3.1. Partial coordination around α

The number of Ω atoms in the 1st coordination shell of α solutes $N_{\alpha-\Omega}$ is given directly from the radius ratio $R = r_\alpha/r_\Omega$ when the 1st shell is occupied by Ω only (Table 1). Kinetic constraints and internal strains produce variability in N via quasi-equivalent clusters [75], so that fractional values of $N_{\alpha-\Omega}$ may be used as a statistical global description. When the 1st shell also contains α atoms, $S(\alpha_\Omega)$ is nonzero and can be used to predict $N_{\alpha-\alpha}$ once the site occupancies $S(\alpha_j)$ are specified. Since $M_{\alpha-\alpha} = 2N_{\alpha-\alpha}$, Eq. (3) can be rearranged as

$$N_{\alpha-\alpha}^{\text{fcc}} = \phi \cdot S(\alpha_\Omega)[S(\alpha_\alpha) + S(\alpha_\beta) + S(\alpha_\gamma)]/\hat{S}_\Omega \quad (4a)$$

$$N_{\alpha-\alpha}^{\text{sc}} = \phi \cdot S(\alpha_\Omega)[S(\alpha_\alpha) + 2S(\alpha_\beta)]/\hat{S}_\Omega \quad (4b)$$

As a simple estimate, $N_{\alpha-\Omega}$ values obtained from the radius ratio R are reduced by $N_{\alpha-\alpha}$ when α and Ω occupy the 1st shell of an α solute. $N_{\alpha-\alpha}$ and $N_{\alpha-\Omega}$ thus calculated show generally good agreement with experiment (Table 5). When both α and Ω atoms occupy the 1st shell, the specific values of $N_{\alpha-\alpha}$ and $N_{\alpha-\Omega}$ are consistent with efficient local atomic packing [28].

Table 5
Experimental and predicted partial coordination numbers

Glass		$N_{\Omega-\Omega}$	$N_{\Omega-\alpha}$	$N_{\alpha-\alpha}$	$N_{\alpha-\Omega}$	Ref.
Ni ₈₁ B ₁₉ $\langle 9 \rangle_{sc}$	Expt.	10.8	2.2	0	9.3	[4]
	Pred.	10.0	1.93	0	8.62	
Ni ₆₄ B ₃₆ $\langle 9 \rangle_{sc}$	Expt.	9.2	4.9	1.1	8.7	[84]
	Pred.	9.07	4.78	1.94	6.67	
Fe ₈₀ B ₂₀ $\langle 9 \rangle_{sc}$	Expt.	12.4	2.16	0	8.64	[85]
	Pred.	10.0	2.11	0	8.52	
Ni ₈₀ P ₂₀ $\langle 10 \rangle_{sc}$	Expt.	9.4	2.33	0	9.3	[76]
	Pred.	10.00	2.50	0	9.80	
Zr ₆₅ Ni ₃₅ $\langle 10 \rangle_{sc}$	Expt.	9.0	2.9	2.3	5.4	[74]
	Pred.	7.50	2.59	1.88	8.65	
Nb ₆₀ Ni ₄₀ $\langle 12 \rangle_{fcc}$	Expt.	9.0	5.5	3.8	8.2	[72]
	Pred.	8.63	6.21	3.44	7.03	
Ni ₆₃ Nb ₃₇ $\langle 16 \rangle_{fcc}$	Expt.	6.6	5.9	5.6	10.0	[72]
	Pred.	10.19	6.56	5.23	11.40	
Al ₉₀ Y ₁₀ $\langle 17 \rangle_{fcc}$	Expt.	10.7 ± 0.8	1.6 ± 0.2	1.2 ± 0.9	14.2 ± 1.3	[86]
	Pred.	11.81	1.47	0.13	17.04	

The intensity of the α - α nearest-neighbor peak and $N_{\alpha-\alpha}$ are related but separate experimental measurements, as the latter is derived from the area under the peak. A single value of $S(\alpha_{\Omega})$ provides good agreement with both $N_{\alpha-\alpha}$ and the intensity of the α - α nearest neighbor peak in Ni₈₁B₁₉, Fe₈₀B₂₀, Ni₈₀P₂₀, Zr₆₅Ni₃₅, Nb₆₀Ni₄₀ (Table 4). $S(\alpha_{\Omega}) = 0.506$ is obtained from the height of the α - α nearest neighbor peak for Ni₆₃Nb₃₇, while $S(\alpha_{\Omega}) = 1.053$ is consistent with the composition and the experimental value of $N_{\alpha-\alpha}$. The width of the Ni₆₃Nb₃₇ α - α nearest neighbor peak is significantly larger than for the other systems, which may contribute to this discrepancy.

4.3.2. Partial coordination around Ω

Species in the 1st shell of a typical Ω can also be estimated from the ECP model. As a rough approximation, an Ω that occupies a common vertex between two adjacent α clusters has q Ω atoms in its first shell from each α cluster, so that $N_{\Omega-\Omega} \approx 2q$ (see the common vertices in Fig. 3b as an illustration). The surface connectivity q [3,77] is defined here as the maximum number of Ω atoms of radius r_{Ω} that may simultaneously contact a given Ω on a curved surface of radius r_{α} . From geometry, $q = 4$ for $0.414 < r_{\alpha}/r_{\Omega} < 0.902$, and $q = 5$ for $r_{\alpha}/r_{\Omega} \geq 0.902$ [3]. In the limit, $q \rightarrow 6$ as $R \rightarrow \infty$. When adjacent α clusters share a common edge or a common face, then $N_{\Omega-\Omega} \approx 2q - 1$ and $N_{\Omega-\Omega} \approx 2q - 2$, respectively. This simple estimate gives a lower bound, especially for clusters with $N < 12$, since 1–3 additional Ω atoms can be accommodated as a result of higher cluster curvature and non-tetrahedral surface packing (Fig. 10). On the other hand, the presence of α_{Ω} defects will decrease the value of $N_{\Omega-\Omega}$. Since vertex sharing between adjacent α clusters is most common, then

$$N_{\Omega-\Omega} \approx 2(q + 1) - S(\alpha_{\Omega})[N_{\alpha-\Omega}/\hat{S}_{\Omega}] \quad (5)$$

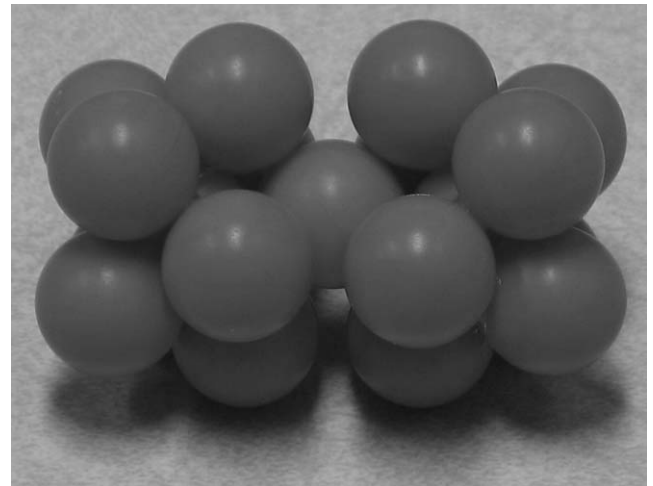


Fig. 10. Two nearest neighbour $N = 9$ clusters sharing an Ω atom at a common vertex with $2q = 8$ nearest neighbour Ω atoms shown. For the cluster conformation shown, two additional nearest neighbour Ω atoms may be inserted. The actual number of additional nearest neighbours that can be accommodated depends sensitively on the cluster topology, the type of cluster sharing, and the specific angular orientation between the two clusters.

Experimental values are broadly consistent with this simple estimate (Table 5).

An idealized visualization is used to develop an estimate of the number of solute atoms i in the 1st shell of a typical Ω atom, $N_{\Omega-i}$. In this idealized structure, β sites constitute vertices of the octahedra and tetrahedra that comprise an fcc lattice, while α and γ sites occupy the centers of these same octahedra and tetrahedra, respectively. Ω sites occupy common vertices between adjacent α clusters, or equivalently occupy the β - β midpoints of the octahedra and tetrahedra edges. Although this idealization places Ω atoms at ordered positions within the structure and hence

contradicts one of the major requirements of the ECP model, it nevertheless correctly represents the number and general location of Ω atoms relative to solutes. From this visualization it can be seen that each Ω atom has approximately two each of α , β and γ sites in the 1st coordination shell. Equations for the actual number of solutes in the 1st shell of a typical Ω atom as an explicit function of cluster packing symmetry and $S(i_j)$ values are developed below.

There are $2[S(i_\alpha) + S(i_\beta) + S(i_\gamma)]$ nearest-neighbor i solutes per β – β midpoint, there are ϕ β – β midpoints that are adjacent to each α site, and there are $N_{\alpha-\Omega}$ Ω atoms adjacent to each α site. Combining these terms gives $2\phi[S(i_\alpha) + S(i_\beta) + S(i_\gamma)]/N_{\alpha-\Omega}$ nearest-neighbor i solutes per Ω atom. A term is added to account for the presence of $S(i_\Omega)$ defects, so that

$$N_{\Omega-i}^{\text{fcc}} = 2\phi[S(i_\alpha) + S(i_\beta) + S(i_\gamma) + (q/\hat{S}_\Omega) \cdot S(i_\Omega)]/N_{\alpha-\Omega} \quad (6a)$$

$$N_{\Omega-i}^{\text{sc}} = 2\phi[S(i_\alpha) + 2S(i_\beta) + (q/\hat{S}_\Omega) \cdot S(i_\Omega)]/N_{\alpha-\Omega} \quad (6b)$$

Binary glasses with vacancy defects have been considered to explore this prediction, including the $\langle 9 \rangle_{\text{sc}}$ glasses $\text{Ni}_{81}\text{B}_{19}$ and $\text{Fe}_{80}\text{B}_{20}$ and the $\langle 10 \rangle_{\text{sc}}$ glass $\text{Ni}_{80}\text{P}_{20}$. Binary glasses with anti-site defects further support this prediction, including $\text{Ni}_{81}\text{B}_{19}$, $\text{Zr}_{65}\text{Ni}_{35}$, $\text{Nb}_{60}\text{Ni}_{40}$, $\text{Ni}_{63}\text{Nb}_{37}$ and $\text{Al}_{90}\text{Y}_{10}$. The same $S(\alpha_j)$ values are used here as were used for MRO predictions of $\text{Ni}_{81}\text{B}_{19}$, $\text{Zr}_{65}\text{Ni}_{35}$, $\text{Nb}_{60}\text{Ni}_{40}$ and $\text{Ni}_{63}\text{Nb}_{37}$ in Section 4.2, so that the same structures are modeled. $S(\alpha_j)$ values used in these predictions are shown in Table 4, and the predicted and measured $N_{\Omega-\alpha}$ values are given in Table 5. Good agreement is generally obtained.

4.4. Density and atomic packing fraction

The density of metallic glasses can be calculated by estimating A_0 (Section 3.3) and by counting the number and type of atoms in a cluster unit cell (Section 4.1). Glass compositions are matched exactly, and the calculated densities are compared with experimental values for a number of topological binary and ternary glasses (Table 6). A

weighted average for the atomic mass of (Ni,Fe) was used for Al–Gd–(Fe,Ni) glasses, and sc cluster packing was used for $\text{Ni}_{81}\text{B}_{19}$. While the errors in calculated density can be as large as 40%, these values depend on A_0^3 , so that these significant density errors represent a smaller errors in A_0 . If the density error is ascribed to uncertainty in A_0 , then 11 of 14 calculations have a A_0 error of less than 10%. The A_0 value needed to obtain agreement with the measured density for $\text{Ni}_{81}\text{B}_{19}$ is very close to the value used to fit the diffraction data. The atomic packing fraction, determined from the volume of the atoms present and the corrected value of A_0 , typically fall within the range between dense random packing (~ 0.64) and fcc packing (~ 0.74) of equal-sized spheres (Table 6).

4.5. Other model predictions

It is a basic feature of the ECP model that all solutes have efficient atomic packing in the 1st coordination shell. An approach to quantify local atomic packing efficiency [46] has been applied to a number of metallic glasses [28]. Efficient atomic packing was found in the 1st coordination shell of solutes within experimental precision. The only exception was for the packing around P atoms in Co–P glasses. Although not specified by the ECP model, it was found that packing around Ω atoms was also generally very efficient.

The ECP model predicts that no more than 4 topologically distinct species occur in a glass structure. The comparisons in Section 4 and in [47] give a broad assessment representing most major families of metallic glasses, some with as many as seven chemically distinct species. Alloys with more than 4 topologically distinct species were not identified.

5. Discussion

5.1. Model features

5.1.1. Efficient atomic packing and cluster ordering

The efficient filling of space in extended systems of unequal spheres is a problem of broad scientific interest

Table 6
Calculated densities and packing fractions

Composition	Actual density (g/cm ³)	Predicted density (g/cm ³)	Density error (%)	A_0 Error (%)	Corrected A_0 (nm)	Packing fraction	Ref.
$\text{Ni}_{81}\text{B}_{19}$	8.4	10.92	30.0	−9.1	0.395	0.7420	[4]
$\text{Pd}_{79.8}\text{Si}_{20.2}$	10.25	13.45	31.2	−9.5	0.663	0.6997	[52]
$\text{Al}_{85}\text{Gd}_6(\text{Fe}_3\text{Ni}_6)$	3.51	3.07	−12.6	4.4	0.928	0.7048	[19]
$\text{Al}_{85}\text{Gd}_8(\text{Fe}_2\text{Ni}_5)$	3.71	3.23	−12.9	4.5	0.927	0.7223	[19]
$\text{Al}_{87}\text{Gd}_6(\text{Fe}_1\text{Ni}_6)$	3.47	2.95	−14.9	5.3	0.920	0.7115	[19]
$\text{Fe}_{70}\text{Zr}_{10}\text{B}_{20}$	7.23	9.52	31.6	9.6	0.855	0.7086	[87]
$\text{Fe}_{70}\text{Nb}_{10}\text{B}_{20}$	7.68	9.07	18.2	−5.7	0.807	0.7183	[87]
$\text{Fe}_{70}\text{Cr}_{10}\text{B}_{20}$	7.34	7.75	5.6	−1.8	0.755	0.7105	[87]
$\text{Mg}_{60}\text{Y}_{10}\text{Cu}_{30}$	3.13	2.71	−13.4	4.7	1.039	0.6784	[88]
$\text{Pd}_{77.5}\text{Cu}_6\text{Si}_{16.5}$	10.48	9.74	−7.1	2.4	0.766	0.7051	[52]
$\text{Pd}_{48}\text{Ni}_{32}\text{P}_{20}$	9.83	6.94	−29.4	11.0	0.768	0.7227	[52]
$\text{Pt}_{52.5}\text{Ni}_{22.5}\text{P}_{25}$	15.85	13.29	−16.1	5.7	0.809	0.6811	[52]
$\text{Zr}_{60}\text{Al}_{10}\text{Cu}_{30}$	6.72	4.60	−31.6	11.9	0.912	0.7254	[21]
$\text{Zr}_{60}\text{Al}_{15}\text{Ni}_{25}$	6.36	4.07	−36.0	13.8	0.896	0.7272	[21]

[78], and the ECP model introduces a new approach to achieve this goal. Local atomic order produced by efficiently-packed solute-centered clusters combined with cluster ordering leads to a number of rather specific model features that provide a simple description of metallic glass structures. However, this is fundamentally a statistical model that does not give precise positions of atoms or clusters. Statistical fluctuations are produced by atomic relaxations resulting from ‘soft’ atoms and packing defects. These relaxations give quasi-equivalent clusters and restrict identifiable cluster order to a length scale of ~ 1 nm or ~ 3 cluster diameters. Nevertheless, the ECP model provides a generalized structural description applicable to the full range of metallic glass topologies that provides new insights and is an attractive alternative to system-specific atomic simulations.

Although atomic clusters have often been proposed, the ECP model gives the first description of ordered cluster packing as a major feature of metallic glass structures. This model provides a simple structural basis for experimentally measured MRO through ordering of solutes at the centers of ordered clusters. While diffraction provides a non-unique basis for generalized structural comparison, diffraction results for solute–solute separations enable a specific, quantitative approach to distinguish the cluster packing symmetry and cluster-cluster separation distances. The present work shows consistently that fcc cluster packing provides best agreement for each of the comparisons with experimental data when the structure-forming clusters have ≥ 12 Ω atoms in the 1st coordination shell, and sc cluster packing when $N_{\alpha-\Omega} < 12$. These same comparisons show that bcc and hcp cluster packing are inconsistent with experimental results. A random distribution of solute-centered clusters is fundamentally inconsistent with experimental observations of solute–solute order.

The possibility of icosahedral cluster packing requires special mention, since this also gives efficient cluster packing. Using a common-neighbor analysis (CNA), a recent computational study of Ni–P, Ni–B and Zr–Pt concludes that icosahedral cluster ordering dominates in those systems [75]. The CNA provides evidence of icosahedral fragments via regular or distorted bicapped pentagonal prisms of clusters with 555, 544 and 433 common-neighbor indices. These represent two neighboring clusters that form, respectively, a bicapped pentagonal prism with five ‘bonds’ between the common neighbors; a distorted bicapped pentagonal prism with four ‘bonds’ amongst the common neighbors; and a distorted bicapped prism with four common clusters that form three ‘bonds’ between the common neighbors. The present work shows that experimental data for the Ni–B and Ni–P systems are well-matched by sc cluster packing with (α_p) defects, giving overall bcc solute symmetry that favors CNA indices of 444. Just as 544 and 433 are distortions of icosahedral ordering, they are also distortions of bcc symmetry. In addition, 555 is a distortion of bcc solute symmetry when

relaxations enable a fifth cluster to become a common neighbor. Thus, the four most intense CNA indices from Sheng et al. are consistent not only with icosahedral ordering but also with bcc solute symmetry, which was not considered by Sheng et al. CNA is a computational tool that attempts to quantify complex spatial relationships, but atomic distortions and ambiguity in the specific symmetry for a given set of CNA indices make a singular determination of cluster ordering difficult. In fact, since ‘order’ implies long-range cluster spacings, it may be inappropriate to assign a definite symmetry given only local distorted cluster positions. A more careful analysis, explicitly considering sc cluster symmetry and looking at specific distortions and symmetry patterns beyond common neighbors, may be required to assess the relative importance of icosahedral and sc cluster symmetry in those simulations.

The utility of such idealizations lies in the ability to predict structure-specific features. By this measure, the ECP model provides a fully satisfactory approach using fcc and sc cluster packing. Icosahedral cluster packing may also be considered within the ECP framework, but it gives a different number of cluster-octahedral and cluster-tetrahedral sites per α site than does sc or fcc cluster packing. For example, an icosahedron of 13 clusters gives 20 cluster-tetrahedral and no cluster-octahedral sites. This provides fewer inter-cluster solute sites and is fundamentally inconsistent with the observation that many metallic glasses have four topologically distinct constituents. Adding a second shell of clusters in one specific configuration (the Mackay icosahedron) does produce 20 cluster-octahedral positions, but 30 additional clusters are required to produce this configuration. Again, the relationship between the number of α clusters and inter-cluster sites is altered, and the spatial extent of cluster order is significantly larger than suggested by experiment. Based on the broad, quantitative agreement with experimental measurements of SRO, MRO, density, composition and the number and size of solute species in a large number of topologically distinct systems, it is concluded that sc and fcc cluster packing described here provides a meaningful representation of metallic glass structures. Icosahedral cluster ordering suggested in simulations of metal–metalloid systems may also provide a reasonable model. Additional detailed studies are required to establish the relative importance of these different cluster packing symmetries.

5.1.2. Representative structural elements

The ECP model has RSEs at two distinct length scales. Efficiently packed solute-centered atomic clusters define a local RSE. Up to three structurally distinct local RSEs (one for each topologically distinct solute) may co-exist in a particular glass structure. A single fcc or sc unit cell of clusters defines a medium-range RSE. This provides a dramatic simplification, and allows the structure of a metallic glass to be reasonably represented by no more than ~ 200 atoms.

5.1.3. Point defects

The presence of point defects is reflected in experimentally measurable features, especially solute–solute p-RDFs and partial coordination numbers. Quantitative predictions from the ECP model rely explicitly on the type and concentration of point defects, providing a strong validation approach. These calculations are independent, and so a specific defect state must give reasonable agreement with all measured quantities. This agreement is achieved here for several different glasses, providing support for the presence of specific defect types. The comparison of predictions with experimental measurements thus provides an important approach for assigning the presence, type and concentrations of point defects.

The comparisons in Section 4 suggest that V_β and V_γ are common defects in topological binary and ternary glasses, and that any solute species can occupy these sites. Anti-site defects on Ω sites, especially α_Ω , provide a structural basis for frequently observed nearest-neighbor solute–solute peaks and give an explanation for glasses where Ω atoms and one of the solutes have nearly equal concentrations. Comparisons here provide no support for important concentrations of V_Ω or V_α . Anti-site occupancy of Ω or other solutes on α sites may occur. Finally, the occupancy of Ω atoms on β or γ sites is not supported.

Good agreement is often achieved with one dominant defect on a given structural site. For example, good agreement is achieved in $\text{Ni}_{81}\text{B}_{19}$ with (α_β) defects and Zr–Al–Ni glasses are most stable when β_γ defects dominate. Some glasses display stability over a wide range of compositions, suggesting that structural sites can be filled progressively, leading to mixed defect states on a single site. Glasses based on Mg and Nd provide two such examples.

5.1.4. Structural diversity

From the discussion in Section 3.1, it can be shown that there are 120 distinct permutations for topological quaternary glasses. Defect states are not necessary to provide an adequate fit to most compositions, and so additional distinct structures where a specific point defect dominates on a given site are not commonly produced in topological quaternary glasses.

There are 45 permutations of solutes for ternary glasses, and at least one of five defect states can occur in each of these structures. For ternary structures comprised of two adjacent occupied coordination states, such as $\langle 15,12 \rangle_{\text{fcc}}$ or $\langle 10,9 \rangle_{\text{sc}}$, α and β sites are filled by their respective solutes and V_γ or β_γ point defects exist. In ternary glasses with an intervening unoccupied coordination state, such as $\langle 15,8 \rangle_{\text{fcc}}$ or $\langle 12,9 \rangle_{\text{fcc}}$, α and β sites can be filled respectively by the larger and smaller solutes, and V_γ or β_γ defects can exist for the next smaller coordination state. Alternatively, the smaller solute may occupy γ sites so that V_β , α_β or γ_β defects occur. The two possible defect states for γ sites in the nine topological ternary glasses with adjacent occupied coordination states produce 18 possible structurally distinct systems. The 36

topological ternary glasses with an intervening unoccupied coordination state will typically display one of the five possible defects listed above for β or γ sites. However, if the third structural sites are filled by vacancies, there is no distinction between structures with V_γ and V_β . Further, if the third structural sites are filled by anti-site defects, a structural distinction is not provided for β_γ or γ_β . Thus, a total of 108 distinct structures can be produced, and a total of 126 distinguishable topological ternary metallic glasses can be specified altogether. While anti-site defects may occur on Ω sites, the random nature of their concentration and distribution make it difficult to specify a topologically distinct structure. Thus, these defects are considered to add to the randomness, but do not produce additional topologically specific structures. Finally, although comparison between model predictions and experimental observations suggest that one type of defect generally dominates in any given ternary glass, combinations of defects may occur, producing additional possibilities to glass structures.

There are 10 distinct binary glass structures. By convention, α sites are filled, so that defects exist on both β and γ sites. Three distinct defect states exist, $(V_\beta + V_\gamma)$, $(\alpha_\beta + V_\gamma)$ and $(\alpha_\beta + \alpha_\gamma)$, so that there are 30 possible distinct binary glass structures. β and γ sites may be filled progressively with additional α solutes, providing a broad range in α concentrations for some glasses. As for ternary structures, α_Ω defects occur but do not introduce topologically distinct structures.

From the discussion above, a large number of distinct metallic glass structures (276 are described here) can be specified. This provides a basis from which the expansive array of topologically distinct metallic glasses can be rationalized. Thus, while the ECP model provides an important simplification for the description of metallic glass structures, it affords significant diversity as well. It is not clear if all of these structures possess comparable stability, or if all have been produced in actual systems.

5.2. Predictive capabilities

The overall agreement for the comparisons with SRO via partial local coordination numbers, MRO, density and the number of topologically distinct solutes in Section 4 is very good and supports the ECP model. Above all, this model provides an ability to reproduce the constitution of a broad range of metallic glasses. While system-specific computations can often give better agreement, the present simple model provides good agreement for both local and global features in an expansive range of topologically and chemically distinct metallic glasses, validating the basic ideas of this simple hard sphere model.

5.2.1. Comparison with the constitution of known metallic glasses

Successful predictions from the ECP model are shown here for $\langle 17,15,8 \rangle_{\text{fcc}}$, $\langle 15,10,8 \rangle_{\text{fcc}}$, $\langle 12,10,9 \rangle_{\text{fcc}}$ and $\langle 10,9,8 \rangle_{\text{sc}}$

quaternary glasses; for $\langle 17,12 \rangle_{\text{fcc}}$, $\langle 17,8 \rangle_{\text{fcc}}$, $\langle 16,12 \rangle_{\text{fcc}}$, $\langle 15,12 \rangle_{\text{fcc}}$, $\langle 15,10 \rangle_{\text{fcc}}$, $\langle 15,8 \rangle_{\text{fcc}}$, $\langle 12,10 \rangle_{\text{fcc}}$, $\langle 12,9 \rangle_{\text{fcc}}$, $\langle 10,9 \rangle_{\text{sc}}$ and $\langle 10,8 \rangle_{\text{sc}}$ ternary structures; and for $\langle 17 \rangle_{\text{fcc}}$, $\langle 16 \rangle_{\text{fcc}}$, $\langle 12 \rangle_{\text{fcc}}$, $\langle 10 \rangle_{\text{sc}}$ and $\langle 9 \rangle_{\text{sc}}$ binary glasses. These include glasses containing from 2 to 7 chemically distinct species based on Zr, Pd, Ca, La, Sm, Y, Nd, Fe, Al, Mg, Fe, Co and Ni. Finally, both bulk and marginal metallic glasses are included in this comparison. The agreement is generally very good. The ability to accurately predict compositions for this inclusive range of metallic glasses is a strong validation of the ECP structural model.

Although the range in predicted concentrations may be as large as $\sim 30\%$ for α solutes, the ranges for β and γ solutes are smaller ($\sim 10\text{--}20\%$). It is generally found that the specific structure and defect state that provide the best match with constitution also provides the best agreement with independent experimental measurements of density, MRO and partial coordination numbers. It is therefore concluded that the compositional flexibility provided by the ECP model is sufficient to enable an accurate description of the richness and complexity offered by metallic glasses, but is not excessively flexible to allow description of any arbitrary composition.

A truly predictive capability for the constitution of metallic glasses is hindered by the lack of a quantitative description of the influence of topologically identical but chemically distinct species on the stability of metallic glasses (Section 5.3). Additional work is required to define a quantitative model for chemical effects on the stability of metallic glasses. Although a specific effort was made to assess a broad range of chemically distinct glasses representing different structures and defect states, the comparisons shown here are not exhaustive. A vast number of other glasses are known. Of the 276 structure/defect combinations described here, only a small portion is included in the present comparisons. While these comparisons provide adequate validation, additional work is required and modifications to the present descriptions may become necessary.

5.2.2. Comparison with MRO

bcc solute symmetry occurs in each of the five glasses considered here. When $N_\alpha \geq 12$, this is achieved via fcc cluster packing with the $\alpha_\beta + \alpha_\gamma$ defect state, and when $N_\alpha < 12$ it is accomplished with sc cluster packing with α_β defects. While these structures seem to be identical, there is a subtle but important difference, since Ω sites are associated only with α sites and do not depend on the number of β or γ solutes in the structure (Section 4.1.1). Thus, a $\langle 12 \rangle_{\text{fcc}}$ structure with $\alpha_\beta + \alpha_\gamma$ defects will have a composition of $A_{60}B_{40}$ and $A_0 = 6.982 \cdot r_\Omega$, while a $\langle 12 \rangle_{\text{sc}}$ structure with α_β defects has a composition of $A_{80}B_{20}$ and a cluster unit cell length exactly half of that of the $\langle 12 \rangle_{\text{fcc}}$ structure. The preference for bcc solute symmetry may result from solute–solute avoidance and a strong preference for solutes to be surrounded by Ω , with which solutes form strong chemical bonds.

5.2.3. Comparison with SRO and density

All four partial coordination numbers in eight topologically distinct binary metallic glasses are predicted, and are typically within experimental error. The discrepancy in predicted density is generally within an error of $\pm 10\%$. Fourteen glasses with up to four chemically distinct species are included in these comparisons.

5.3. Chemical effects

The ECP model relies implicitly upon chemical effects, since strong solute–solvent bonding is required to form solute-centered clusters with Ω atoms only in the first coordination shell. This is consistent with the large negative enthalpy of mixing between constituents and strong chemical SRO in metallic glasses. The magnitude of solute–solite interactions is also expected to be important, since an interaction energy between solutes that is significantly larger than solute–solvent bonding may produce solute clustering and will reduce the number of Ω atoms that are bound to a given number of solute atoms. Metallic glasses may therefore be considered as structures that display maximal binding of Ω atoms by a minimal number of solutes through a maximal solute dispersion. The importance of balancing the magnitude of chemical interactions has been previously discussed [79]. Quantified relationships to describe this balance in chemical bonding have not yet been developed.

Specific combinations of topologically identical solutes sometimes provide a dramatic difference in glass stability, and this is most likely the result of a chemical effect. For example, (Cu + Ni) in Zr and Pd glasses, (Ti + Al) in Zr glasses and (C+B) in Fe glasses provide superior stability relative to glasses with an equal concentration of only one of these solutes. The basis by which topologically equivalent but chemically distinct solutes may influence the stability of an amorphous alloy has been discussed generally [62] but is still not established.

5.4. Atomic radii

While interatomic separations in crystalline solids can be determined with an accuracy of up to five significant digits, there is no rigorous approach for assigning a particular portion of this distance to one atom and the remainder to the other, especially between different atomic species. Further, interatomic separations depend upon the local structure, chemistry and bond type. The basis and validity of representing atoms as spheres with a single set of atomic radii independent of local structure and chemistry has a rich history (see Chapter 7 of [80]) but must nevertheless be considered for the present case.

Tabulations attempt to account for local structure and chemistry by providing a single set of atomic radii that best fit observed atom separations in a large number of condensed solids. This is clearly an approach of convenience, as there is ample evidence of important differences in

atomic size and shape in different atomic environments. Large differences in atomic radii are obtained for different coordination states in solids dominated by ionic and covalent bonding, so that explicit account of local structure can be essential. Nevertheless, an error of ~ 5 pm [81] or a few percent [82] is assessed for a single set of atomic radii that includes ionic, covalent and metallic bonded solids. When used with care this approach enables a dramatic simplification that provides a foundation for many well-established models in condensed solids.

The basis for the atomic radii used here is a critical evaluation of experimental values in metallic glasses [30]. This earlier dataset is extended here by critical analysis of atomic separations in [83] for atom pairs in intermetallic compounds compositionally similar to selected glasses, where atomic bonding and local coordination are expected to be similar [2,5]. This dataset is obtained from solids dominated by a specific bonding state (metallic and partial covalency). Atomic radii in metals are far less sensitive to structure and chemistry than are ionic or covalent solids, so that errors for this dataset are expected to be smaller than for datasets fit to solids with broader differences in bonding type and structures. The use of radius ratios rather than absolute values further reduces errors associated with a hard sphere assumption in the present case. An assessed error of $\pm 2\%$ in radius ratios, R , is used here. This gives a modest bound to account for uncertainties in atom size, and provides reasonably consistent results within the present work. Atomic radii obtained from this critical analysis are given in Table 2.

6. Summary

The efficient cluster packing (ECP) model is developed and validated for the structure of metallic glasses. Efficiently packed solute-centered atomic clusters are densely packed to efficiently fill space. Four rules summarize the major features of the ECP model that provide statistical preferences for the major structural features.

1. *The basic structure is formed by a dense packing of efficiently packed solute-centered atomic clusters with solvent atoms only in the 1st coordination shell.* A good fit to experimental data is achieved with fcc cluster packing when the structure-forming clusters have ≥ 12 solvent atoms (Ω) in the 1st coordination shell, and sc cluster packing dominates when there are < 12 Ω atoms in the 1st shell. In addition to Ω and the primary cluster-forming solutes (α), two additional topologically distinct sites and species are produced – one on cluster-octahedral sites (β) and one on cluster-tetrahedral sites (γ). By convention, the structure-forming solute is the largest solute species, followed by β and γ . Solute occupy ordered positions as a consequence of this rule, but internal strains degrade order beyond a length scale of ~ 1 nm, or about one cluster unit cell. As a result of site ordering, point defects can exist within the structure.

2. *Adjacent structure-forming clusters overlap in the 1st coordination shell.* Vertex sharing is preferred to minimize internal strains. Edge- and vertex-sharing exists between unlike clusters.
3. *There is no orientational order amongst clusters.* This enforces randomness of the solvent atoms that is required by the defining feature of metallic glasses.
4. *All solutes have specific radius ratios R^* relative to solvent atoms, so that all solutes form efficiently-packed solute-centered atomic clusters.* Atoms with radius ratios R within $\pm 2\%$ of one another are considered to be topologically equivalent.

The ECP model relies upon solute-centered clusters with solvent atoms only in the first coordination shell as local RSEs, and introduces a single cluster unit cell as a RSE at a medium range length scale. Cluster ordering provides a physical basis for medium range atomic order (MRO). Point defects are established as important structural features. A locally-distributed free volume sufficient to accept an additional atom, termed a ‘vacancy’ here for convenience, and solute anti-site defects on β and γ sites are common, as well as α anti-site occupancy of Ω sites. Structural diversity is provided from permutations of different solute sizes and point defects, and 276 topologically distinct structures are described. A structurally specific nomenclature is devised from the local coordination numbers of the solutes present.

The ECP model provides an ability to quantitatively predict specific structural information over local, medium-range and global length scales. Predictions are given for partial coordination numbers, MRO, density and the number, sizes and concentrations of constituents. Each distinct structure and defect state gives a unique prediction for these quantities, providing an approach to distinguish structure and defect state by comparison with experimental data. The agreement between experiment and predictions is good in all of these areas. This is a topological model, constructed by explicitly addressing only relative atomic size of the constituents. However, chemical effects provide an important contribution to metallic glass stability, and internal strains may also influence stability. The present model is not fully predictive, and quantitative relationships describing chemical effects and internal strains are required. Nevertheless, the predictive capability of this model offers general guidance for the discovery of new metallic glasses.

The efficient filling of space is a problem of broad scientific and practical importance. The present work develops a new packing scheme for extended systems of unequal spheres that may provide insight into other problems where this is important. The basic features of the ECP model may give new insights into other studies in metallic glasses, including the initiation and propagation of deformation, the distribution and nature of free volume, specific mechanisms of mass transport and the nucleation and growth of crystalline phases.

A single topological model constructed with a small number of simple rules is able to reasonably represent several major experimental observations in metallic glasses. It is concluded that the ECP model is an accurate representative model of the main structural features that dominate in metallic glasses.

Acknowledgements

I thank Dr. O. Senkov for the initial insight into the importance of relative atomic sizes in the structure of metallic glasses and for many insightful discussions. I also acknowledge useful questions and comments from many colleagues, especially Profs. P. Gupta (who pointed out that Eq. (1) is valid only for vertex-sharing nearest neighbor α clusters), S. Ranganathan, P. Harrowell, K. Kelton and L. Greer. This research was supported under the DARPA Structural Amorphous Metals Initiative (Dr. L. Christodoulou, Program Manager) and Air Force Office of Scientific Research Task 01ML05-COR (Dr. J. Tiley, Program Manager).

Appendix A. Determination of cluster unit cell length

The unit vector lengths A_{hkl} for adjacent face sharing nearest-neighbor clusters with fcc cluster-packing symmetry in an ideal cluster unit cell where all α , β and γ sites are occupied by their respective solutes are given as:

$$A_{100,f}^{\text{fcc}} = 2r_{\Omega} \left\{ \sqrt{(R_{\alpha} + 1)^2 - 4/3} + \sqrt{(R_{\beta} + 1)^2 - 4/3} \right\} \quad (\text{A1(a)})$$

$$A_{110,f}^{\text{fcc}} = 4r_{\Omega} \left\{ \sqrt{(R_{\alpha} + 1)^2 - 4/3} \right\} \quad (\text{A1(b)})$$

$$A_{111,f}^{\text{fcc}} = 2r_{\Omega} \left\{ \sqrt{(R_{\alpha} + 1)^2 - 4/3} + \sqrt{(R_{\beta} + 1)^2 - 4/3} + 2\sqrt{(R_{\gamma} + 1)^2 - 4/3} \right\} \quad (\text{A1(c)})$$

When adjacent clusters share a common edge, these distances are increased slightly:

$$A_{100,e}^{\text{fcc}} = 2r_{\Omega} \left\{ \sqrt{(R_{\alpha} + 1)^2 - 1} + \sqrt{(R_{\beta} + 1)^2 - 1} \right\} \quad (\text{A1(d)})$$

$$A_{110,e}^{\text{fcc}} = 4r_{\Omega} \left\{ \sqrt{(R_{\alpha} + 1)^2 - 1} \right\} \quad (\text{A1(e)})$$

$$A_{111,e}^{\text{fcc}} = 2r_{\Omega} \left\{ \sqrt{(R_{\alpha} + 1)^2 - 1} + \sqrt{(R_{\beta} + 1)^2 - 1} + 2\sqrt{(R_{\gamma} + 1)^2 - 1} \right\} \quad (\text{A1(f)})$$

Finally, these lengths increase further when a common vertex is shared, so that:

$$A_{100,v}^{\text{fcc}} = 2r_{\Omega} \{R_{\alpha} + R_{\beta} + 2\} \quad (\text{A1(g)})$$

$$A_{110,v}^{\text{fcc}} = 4r_{\Omega} \{R_{\alpha} + 1\} \quad (\text{A1(h)})$$

$$A_{111,v}^{\text{fcc}} = 2r_{\Omega} \{R_{\alpha} + R_{\beta} + 2R_{\gamma} + 4\} \quad (\text{A1(i)})$$

Table A1 provides reduced cluster unit cell lengths (A_0 normalized by the solvent atom radius r_{Ω}) for an idealized cluster unit cell obtained from the unit vector lengths A_{100} , ($A_{110}/\sqrt{2}$) and ($A_{111}/\sqrt{3}$). The radius ratios used in the calculations are $R_{\alpha} = 0.902$, $R_{\beta} = 0.799$ and $R_{\gamma} = 0.710$, representing a $\langle 12,10,9 \rangle_{\text{fcc}}$ structure. This topology represents the Vitreloy family of bulk metallic glasses based on Zr that also contain Be. The cluster unit cell length is $6.251(r_{\Omega})$, since this is the largest value for face-sharing adjacent unlike clusters. The unit cell length for a Zr-based glass ($r_{\text{Zr}} = 0.158$ nm) with this ideal structure is 0.988 nm.

Appropriate modifications to Eq. (A1) are required to determine the unit lengths in defective structures. For convenience, the following discussion assumes that all equivalent structural sites share the same defect. This assignment is chosen for simplicity, and it is possible that partial or mixed defects exist on a given site. The discussion below further assumes that there are no defects on Ω or α sites, and that γ sites will be vacant if β sites are vacant.

The unit vector lengths in structures with anti-site solute defects are given by a simple substitution of the appropriate reduced radius ratios in Eq. (1). For example, if β and γ sites are both fully occupied by β solutes, then R_{β} is used in place of R_{γ} in Eq. (A1). Similarly, if α , β and γ sites are all occupied by α solutes, then R_{α} is substituted for both R_{β} and R_{γ} .

Modifications are required to Eq. (A1) for vacancy defects. Imagine next nearest neighbor clusters that share faces with a common co-linear third cluster. This configuration is simplified as two trigonal bipyramids that share a common middle solute atom (Fig. A1a). The two equilateral triangular arrangements of Ω atoms are in parallel planes, and the separation between these planes δ decreases as the size of the middle solute decreases. A minimum separation is achieved when the middle solute has a reduced radius of $R = 0.4142$ and occupies the center of an octahedron of Ω atoms. The system is ‘jammed’ and further decrease in the size of the middle solute will not allow the two trigonal Ω arrays, and hence the two bounding clusters, to come in closer contact (Fig. A1 b). The minimum separation between parallel faces of two next-nearest neighbor clusters with an intervening vacant solute site is thus given by the perpendicular separation of parallel faces of an octahedron, $\delta^f = r_{\Omega}(2\sqrt{2}/\sqrt{3})$.

A similar development can be provided for the closest approach between next-nearest neighbor clusters that share edges with a common intervening cluster (Fig. A2a). The ‘jammed’ configuration in this case is an Ω tetrahedron, and the limiting approach is the perpendicular separation

Table A1
Reduced cluster unit cell lengths for the $\langle 12,10,9 \rangle$ structure

α_0	Face	Edge	Vertex
A_{100}/r_{Ω}	5.782	6.227	7.402
$A_{110}/(\sqrt{2}r_{\Omega})$	4.276	4.577	5.380
$A_{111}/(\sqrt{3}r_{\Omega})$	6.251	6.799	8.223

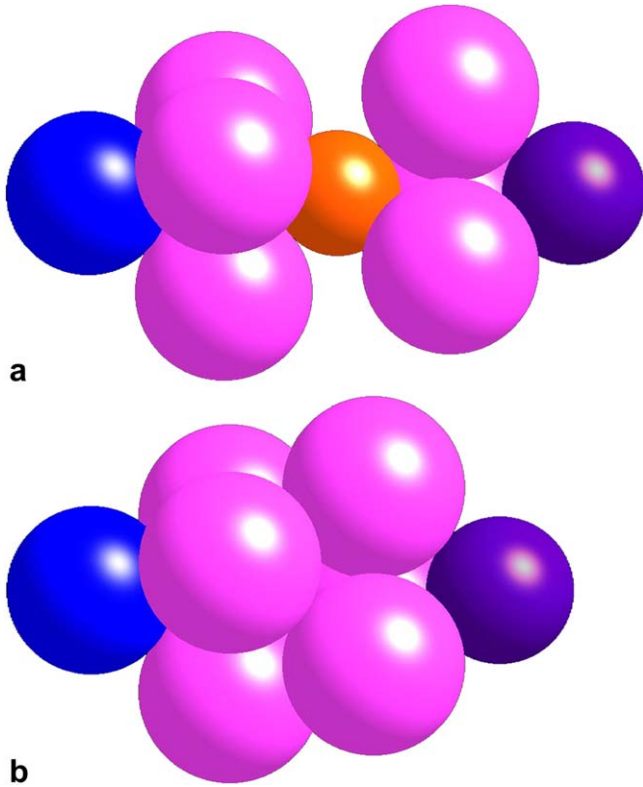


Fig. A1. Illustration of the closest approach for next-nearest neighbor α and β clusters that share faces with a common intervening co-linear γ cluster. Only solvent atoms that are common between nearest neighbor solutes are shown for clarity. (a) α and β next-nearest neighbors separated by a γ solute, simplified as two trigonal bipyramids sharing the common γ atom. (b) The configuration produced by placing a vacancy in the γ solute position, illustrating the closest approach between the α and β solutes in this 'jammed' configuration.

between two non-contacting edges of a tetrahedron, $\delta^e = r_\Omega \sqrt{2}$ (Fig. A2b). The closest approach for next-nearest neighbor clusters that share vertices with a common intervening cluster possessing a vacant central solute is simply given as $\delta^v = 2r_\Omega$.

These results are incorporated in Eq. (A2) for a structure where all γ sites are vacant. The distances along $\langle 100 \rangle$ and $\langle 110 \rangle$ are unchanged, since neither of these directions contains a term for R_γ . The vertex sharing relation for the $\langle 111 \rangle$ direction is changed so that R_γ is removed. In the remaining two equations, the terms containing R_γ are replaced with δ^f for face-sharing, and δ^e for edge-sharing. Thus, for a structure where all γ sites are vacant:

$$A_{100,f}^{\text{fcc}} = 2r_\Omega \left\{ \sqrt{(R_\alpha + 1)^2 - 4/3} + \sqrt{(R_\beta + 1)^2 - 4/3} \right\} \quad (\text{A2(a)})$$

$$A_{110,f}^{\text{fcc}} = 4r_\Omega \left\{ \sqrt{(R_\alpha + 1)^2 - 4/3} \right\} \quad (\text{A2(b)})$$

$$A_{111,f}^{\text{fcc}} = 2r_\Omega \left\{ \sqrt{(R_\alpha + 1)^2 - 4/3} + \sqrt{(R_\beta + 1)^2 - 4/3} + (2\sqrt{2}/\sqrt{3}) \right\} \quad (\text{A2(c)})$$

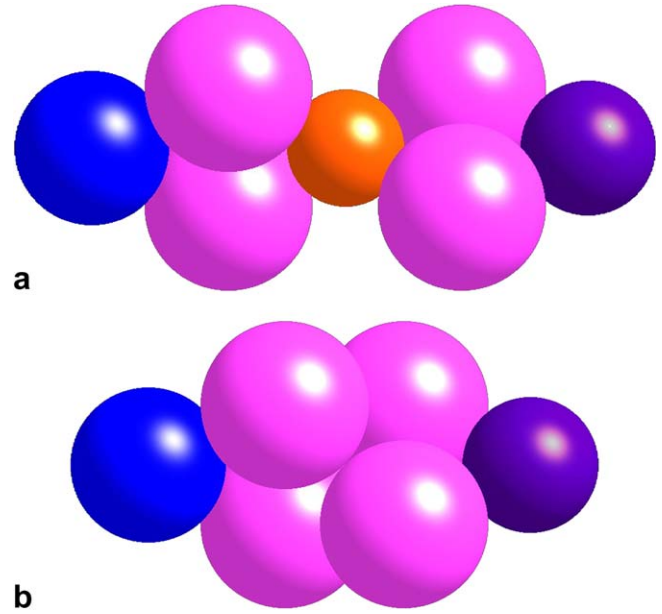


Fig. A2. Illustration of next-nearest neighbor α and β clusters that share edges with a common intervening co-linear γ cluster. (a) This configuration is simplified by showing only the α , γ and β solute atoms and the Ω atoms that are common between adjacent clusters. (b) The configuration produced by placing a vacancy in the γ solute position, illustrating the closest approach between the α and β solutes in this 'jammed' configuration.

$$A_{100,e}^{\text{fcc}} = 2r_\Omega \left\{ \sqrt{(R_\alpha + 1)^2 - 1} + \sqrt{(R_\beta + 1)^2 - 1} \right\} \quad (\text{A2(d)})$$

$$A_{110,e}^{\text{fcc}} = 4r_\Omega \left\{ \sqrt{(R_\alpha + 1)^2 - 1} \right\} \quad (\text{A2(e)})$$

$$A_{111,e}^{\text{fcc}} = 2r_\Omega \left\{ \sqrt{(R_\alpha + 1)^2 - 1} + \sqrt{(R_\beta + 1)^2 - 1} + \sqrt{2} \right\} \quad (\text{A2(f)})$$

$$A_{100,v}^{\text{fcc}} = 2r_\Omega \{R_\alpha + R_\beta + 2\} \quad (\text{A2(g)})$$

$$A_{110,v}^{\text{fcc}} = 4r_\Omega \{R_\alpha + 1\} \quad (\text{A2(h)})$$

$$A_{111,v}^{\text{fcc}} = 2r_\Omega \{R_\alpha + R_\beta + 4\} \quad (\text{A2(i)})$$

Similar changes are made for vacant β and γ sites and are given in Eq. (A3):

$$A_{100,f}^{\text{fcc}} = 2r_\Omega \left\{ \sqrt{(R_\alpha + 1)^2 - 4/3} + (\sqrt{2}/\sqrt{3}) \right\} \quad (\text{A3(a)})$$

$$A_{110,f}^{\text{fcc}} = 4r_\Omega \left\{ \sqrt{(R_\alpha + 1)^2 - 4/3} \right\} \quad (\text{A3(b)})$$

$$A_{111,f}^{\text{fcc}} = 2r_\Omega \left\{ \sqrt{(R_\alpha + 1)^2 - 4/3} + (3\sqrt{2}/\sqrt{3}) \right\} \quad (\text{A3(c)})$$

$$A_{100,e}^{\text{fcc}} = 2r_\Omega \left\{ \sqrt{(R_\alpha + 1)^2 - 1} + (1/\sqrt{2}) \right\} \quad (\text{A3(d)})$$

$$A_{110,e}^{\text{fcc}} = 4r_\Omega \left\{ \sqrt{(R_\alpha + 1)^2 - 1} \right\} \quad (\text{A3(e)})$$

$$A_{111,e}^{\text{fcc}} = 2r_\Omega \left\{ \sqrt{(R_\alpha + 1)^2 - 1} + (3/\sqrt{2}) \right\} \quad (\text{A3(f)})$$

$$A_{100,v}^{\text{fcc}} = 2r_\Omega \{R_\alpha + 2\} \quad (\text{A3(g)})$$

Table A2

Reduced cluster unit cell lengths for the $\langle 12,10 \rangle$ structure with vacant γ sites

α_0	Face	Edge	Vertex
A_{100}/r_Ω	5.782	6.227	7.402
$A_{110}/(\sqrt{2}r_\Omega)$	4.276	4.577	5.380
$A_{111}/(\sqrt{3}r_\Omega)$	5.224	5.228	6.583

Table A3

Reduced cluster unit cell lengths for the $\langle 12 \rangle$ structure with vacant ($\beta + \gamma$) sites

α_0	Face	Edge	Vertex
A_{100}/r_Ω	4.656	4.650	5.804
$A_{110}/(\sqrt{2}r_\Omega)$	4.276	4.577	5.380
$A_{111}/(\sqrt{3}r_\Omega)$	4.574	4.318	5.661

$$A_{110,v}^{\text{fcc}} = 4r_\Omega\{R_\alpha + 1\} \quad (\text{A3(h)})$$

$$A_{111,v}^{\text{fcc}} = 2r_\Omega\{R_\alpha + 4\} \quad (\text{A3(i)})$$

The results from Eqs. (A2) and (A3) and are given in Tables A2 and A3. In both tables $R_\alpha = 0.902$ and in Table A2 $R_\beta = 0.799$, so that $\langle 12,10 \rangle_{\text{fcc}}$ and $\langle 12 \rangle_{\text{fcc}}$ structures are shown in Tables A2 and A3, respectively. The direction that controls the value of A_0 changes from $\langle 111 \rangle$ for the ideal structure to $\langle 100 \rangle$ for structures with vacancies.

The equations above are generally valid, but additional geometric constraints will modify these results in isolated cases. For example, the minimum separation for adjacent edge-sharing icosahedra is larger than the values given in Eqs. (A1(e)), (A2(e)) and (A3(e)) due to an interference between other Ω atoms in the 1st coordination shell. Conditions where such constraints occur are uncommon for known atomic clusters, and so the equations given here are expected to provide good estimates of the cluster unit cell length A_0 .

Equations have been developed for sc cluster packing using a similar analysis, and are provided in Eq. (A4) for structures where the α and β sites are fully occupied by their respective solutes, and in Eq. (A5) for structures where the β sites are vacant.

$$A_{100,f}^{\text{sc}} = 4r_\Omega \left\{ \sqrt{(R_\alpha + 1)^2 - 4/3} \right\} \quad (\text{A4(a)})$$

$$A_{110,f}^{\text{sc}} = 2r_\Omega \left\{ \sqrt{(R_\alpha + 1)^2 - 4/3} + \left(\sqrt{2}/\sqrt{3} \right) \right\} \quad (\text{A4(b)})$$

$$A_{111,f}^{\text{sc}} = 2r_\Omega \left\{ \sqrt{(R_\alpha + 1)^2 - 4/3} + \sqrt{(R_\beta + 1)^2 - 4/3} \right\} \quad (\text{A4(c)})$$

$$A_{100,e}^{\text{sc}} = 2r_\Omega \left\{ \sqrt{(R_\alpha + 1)^2 - 1} \right\} \quad (\text{A4(d)})$$

$$A_{100,e}^{\text{sc}} = 2r_\Omega \left\{ \sqrt{(R_\alpha + 1)^2 - 1} + \left(1/\sqrt{2} \right) \right\} \quad (\text{A4(e)})$$

$$A_{111,e}^{\text{sc}} = 2r_\Omega \left\{ \sqrt{(R_\alpha + 1)^2 - 1} + \sqrt{(R_\beta + 1)^2 - 1} \right\} \quad (\text{A4(f)})$$

$$A_{100,v}^{\text{sc}} = 2r_\Omega\{R_\alpha + 1\} \quad (\text{A4(g)})$$

$$A_{110,v}^{\text{sc}} = 2r_\Omega\{R_\alpha + 2\} \quad (\text{A4(h)})$$

$$A_{111,v}^{\text{sc}} = 2r_\Omega\{R_\alpha + R_\beta + 2\} \quad (\text{A4(i)})$$

$$A_{100,f}^{\text{sc}} = 4r_\Omega \left\{ \sqrt{(R_\alpha + 1)^2 - 4/3} \right\} \quad (\text{A5(a)})$$

$$A_{110,f}^{\text{sc}} = 2r_\Omega \left\{ \sqrt{(R_\alpha + 1)^2 - 4/3} + \left(\sqrt{2}/\sqrt{3} \right) \right\} \quad (\text{A5(b)})$$

$$A_{111,f}^{\text{sc}} = 2r_\Omega \left\{ \sqrt{(R_\alpha + 1)^2 - 4/3} + \left(\sqrt{2}/\sqrt{3} \right) \right\} \quad (\text{A5(c)})$$

$$A_{100,e}^{\text{sc}} = 2r_\Omega \left\{ \sqrt{(R_\alpha + 1)^2 - 1} \right\} \quad (\text{A5(d)})$$

$$A_{110,e}^{\text{sc}} = 2r_\Omega \left\{ \sqrt{(R_\alpha + 1)^2 - 1} + \left(1/\sqrt{2} \right) \right\} \quad (\text{A5(e)})$$

$$A_{111,e}^{\text{sc}} = 2r_\Omega \left\{ \sqrt{(R_\alpha + 1)^2 - 1} + \left(1/\sqrt{2} \right) \right\} \quad (\text{A5(f)})$$

$$A_{100,v}^{\text{sc}} = 2r_\Omega\{R_\alpha + 1\} \quad (\text{A5(g)})$$

$$A_{110,v}^{\text{sc}} = 2r_\Omega\{R_\alpha + 2\} \quad (\text{A5(h)})$$

$$A_{111,v}^{\text{sc}} = 2r_\Omega\{R_\alpha + 2\} \quad (\text{A5(i)})$$

References

- [1] Klement W, Willens RH, Duwez P. Nature 1960;187:869.
- [2] Gaskell PH. Models for the structure of amorphous solids. In: Zarzycki J, editor. Materials science and technology. Glasses and amorphous materials, vol. 9. Cambridge, UK: VCH; 1991. p. 175.
- [3] Miracle DB, Sanders WS, Senkov ON. Philos Magn A 2003;83:2409.
- [4] Lamparter P, Sperl W, Steeb S, Bletty J. Z Naturforsch 1982;37a:1223.
- [5] Gaskell PH. Models for the structure of amorphous metals. In: Beck H, Guntherodt H-J, editors. Topics in Applied Physics—Glassy metals II, vol. 53. Berlin, Germany: Springer-Verlag; 1983. p. 5.
- [6] Gaskell PH. J Phys C-Solid State Phys 1979;12:4337.
- [7] Dubois JM, LeCaer G. Acta Metall 1984;32:2101.
- [8] Cervinka L. J Non-Cryst Solids 1987;90:371.
- [9] Petkov V, Apostolov A. J Non-Cryst Solids 1990;122:262.
- [10] Lamparter P, Steeb S, Grallath E. Z Naturforsch 1983;38a:1210.
- [11] Cervinka L. J Non-Cryst Solids 1993;156–158:94.
- [12] Dubois J-M, Montoya F, Back C. Mater Sci Eng A 1994;178: 285.
- [13] Hirotsu Y, Matsushita M, Ohkubo T, Makino A, Oikawa T. Mater Sci Eng A 1997;226–228:274.
- [14] Zhang L, Wu Y, Bian X, Li H, Wang W, Li J, et al. J Phys-Condens Matter 1999;11:7957.
- [15] Zhang L, Wu Y, Bian X, Li H, Wang W, Wu S. J Non-Cryst Solids 2000;262:169.
- [16] Sietsma J, Thijsse BJ. J Non-Cryst Solids 1991;135:146.
- [17] Lamparter P, Steeb S. Structure of amorphous and molten alloys. In: Gerold V, editor. Structure of solids, vol. 1. Weinheim, Germany: VCH; 1993. p. 217.
- [18] Hufnagel TC, Brennan S. Phys Rev B 2003;67:014203.
- [19] Dougherty GM, He Y, Shiflet GJ, Poon SJ. Scr Metall Mater 1994;30:101.
- [20] Yavari AR, Uriarte JL, Inoue A. Mater Sci Forum 1998;269–272:533.
- [21] Yavari AR, Inoue A. In: Johnson WL, Liu CT, Inoue A, editors. Bulk metallic glasses. Mater. Res. Soc. Symp, vol. 554. Materials Research Society; 1999. p. 21.
- [22] Inoue A. Mater Sci Eng A 1999;267:171.
- [23] Ramachandrarao P. Z Metallkunde 1980;71:172.
- [24] Battezzati L, Baricco M. J Less Common Metals 1988;145:31.

- [25] Jin O, Schwarz RB, Alamgir FM, Jain H. In: Gonis A, Turchi PEA, Ardell AJ, editors. *Nucleation and growth processes in materials*, vol. 580. Pittsburgh (PA), USA: Mater. Res. Soc. (MRS); 2000. p. 277.
- [26] Mukherjee S, Schroers J, Zhou Z, Johnson WL, Rhim W-R. *Acta Mater* 2004;52:3689.
- [27] Yavari AR. *Phys Lett* 1983;95A:165.
- [28] Miracle DB. *J Non-Cryst Solids* 2004;242:89.
- [29] Polk DE, Giesen BC. In: Gilman JJ, Leamy JH, editors. *Metallic glasses*. ASM International; 1978. p. 1.
- [30] Egami T, Waseda Y. *J Non-Cryst Solids* 1984;64:113.
- [31] Cahn RW. *Metallic glasses*. In: Zarzycki J, editor. *Materials science and technology. Glasses and amorphous materials*, vol. 9. Cambridge, UK: VCH; 1991. p. 493.
- [32] Inoue A. *Mater Sci Eng A* 1997;226–228:357.
- [33] Senkov ON, Miracle DB. *Mater Res Bull* 2001;36:2183.
- [34] Miracle DB, Senkov ON. In: Hanada S, Masahashi N, editors. *Proc. fourth Pacific RIM int. conf. on advanced materials and processing (PRICM4)*, vol. II. Tokyo, Japan: The Japan Institute of Metals; 2001. p. 2893.
- [35] Senkov ON, Miracle DB. *J Non-Cryst Solids* 2003;317:34.
- [36] Gaskell PH. *Nature* 1978;276:484.
- [37] Gaskell PH. *J Non-Cryst Solids* 1979;32:207.
- [38] Dubois JM, Gaskell PH, Caer GL. *Proc Roy Soc A* 1985;402:323.
- [39] Briant CL, Burton JJ. *Phys Stat Sol (b)* 1978;85:393.
- [40] Matsubara E, Harada K, Waseda Y, Chen HS, Inoue A, Masumoto T. *J Mater Sci* 1988;23:753.
- [41] Holland-Moritz D, Schenk T, Simonet V, Bellissent R, Convert P, Hansen T, et al. *Mater Sci Eng A* 2004;375–377:98.
- [42] Luo WK, Sheng HW, Alamgir FM, Bai JM, He JH, Ma E. *Phys Rev Lett* 2004;92:145502.
- [43] Jonsson H, Andersen HC. *Phys Rev Lett* 1988;60:2295.
- [44] Qi DW, Wang S. *Phys Rev B* 1991;44:884.
- [45] Wang X-D, Qi M, Dong C. *Chin Phys Lett* 2003;20:891.
- [46] Miracle DB, Senkov ON. *J Non-Cryst Solids* 2003;319:174.
- [47] Miracle DB. *Nat Mater* 2004;3:697.
- [48] Miracle DB, Lord EA, Ranganathan S. *Trans JIM* 2006;47:1737.
- [49] Mackay AL, Finney JL, Gotoh K. *Acta Crystallogr A* 1977;33:98.
- [50] Clare BW, Kepert DL. *J Math Chem* 1991;6:325.
- [51] Stephens PW. *The icosahedral glass model*. In: Jaric MV, Gratias D, editors. *Extended icosahedral structures*, vol. 3. Boston (MA), USA: Academic Press; 1989. p. 37.
- [52] Ramachandrarao P, Cantor B, Cahn RW. *J Mater Sci* 1977;12:2488.
- [53] Amiya K, Inoue A. *Mater Trans JIM* 2002;43:81.
- [54] Amiya K, Inoue A. *Mater Trans JIM* 2002;43:2578.
- [55] Senkov ON, Scott JM. *Scr Mater* 2004;50:449.
- [56] Senkov ON, Scott JM. *Mater Lett* 2004;58:1375.
- [57] Guo FQ, Poon SJ, Shiflet GJ. *Appl Phys Lett* 2004;84:37.
- [58] Park ES, Kim DH. *J Mater Res* 2004;19:685.
- [59] Fan GJ, Loser W, Roth S, Eckert J. *Acta Mater* 2000;48:3823.
- [60] Inoue A, Takeuchi A, Zhang T. *Metall Mater Trans* 1998;29A:1779.
- [61] Inoue A, Nakamura T, Sugita T, Zhang T, Masumoto T. *Mater Trans JIM* 1993;34:351.
- [62] Guo F, Poon SJ, Shiflet GJ. *Appl Phys Lett* 2003;83:2575.
- [63] Kim SH, Inoue A, Masumoto T. *Mater Trans JIM* 1990;31:929.
- [64] Louzguine DV, Kawamura Y, Inoue A. *Mater Sci Forum* 2000;350–351:123.
- [65] Inoue A, Nakamura T, Nishiyama N, Masumoto T. *Mater Trans JIM* 1992;33:937.
- [66] He Y, Shen T, Schwarz R. *Metall Mater Trans* 1998;29A:1795.
- [67] Inoue A. *Acta Mater* 2000;48:279.
- [68] Kramer M, Besser MJ, Yang N, Rozhkova E, Sordellet DJ, Zhang Y, et al. *J Non-Cryst Solids* 2003;317:62.
- [69] Ponnambalam V, Poon SJ, Shiflet GJ, Keppens VM, Taylor R, Petculescu G. *Appl Phys Lett* 2003;83:1131.
- [70] Ponnambalam V, Poon SJ, Shiflet GJ. *J Mater Res* 2004;19:1320.
- [71] Inoue A. *Prog Mater Sci* 1998;43:365.
- [72] Steeb S, Lamparter P. *J Non-Cryst Solids* 1993;156–158:24.
- [73] Fukunaga T, Watanabe N, Suzuki K. *J Non-Cryst Solids* 1984;61 and 62:343.
- [74] Lee A, Etherington G, Wagner CNJ. *J Non-Cryst Solids* 1984;61–62:349.
- [75] Sheng HW, Luo WK, Alamgir FM, Bai JM, Ma E. *Nature* 2006;439:419.
- [76] Lamparter P. *Phys Scr* 1995;T57:72.
- [77] Frank FC, Kasper JS. *Acta Crystallogr* 1958;11:184.
- [78] Aste T, Weaire D. *The pursuit of perfect packing*. Bristol, UK: Institute of Physics; 2000.
- [79] Poon SJ, Shiflet GJ, Guo FQ, Ponnambalam V. *J Non-Cryst Solids* 2003;317:1.
- [80] Pauling L. *The nature of the chemical bond*. Ithaca (NY): Cornell University Press; 1960.
- [81] Slater JC. *J Chem Phys* 1964;41:3199.
- [82] Kittel C. *Introduction to solid state physics*. New York (NY): Wiley; 1976.
- [83] Daams JLC, Villars P, van Vucht JHN. *Atlas of crystal structure types for intermetallic phases*. Metals Park (OH): ASM International; 1991.
- [84] Cowlam N, Guoan W, Gargner PP, Davies HA. *J Non-Cryst Solids* 1984;61 and 62:337.
- [85] Nold E, Lamparter P, Olbrich H, Rainer-Harbach G, Steeb S. *Z Naturforsch* 1981;36a:1032.
- [86] Matsubara E, Waseda Y, Inoue A, Ohtera H, Masumoto T. *Z Naturforsch* 1989;44a:814.
- [87] Matsubara E, Sato S, Imafuku M, Nakamura T, Koshiha H, Inoue A, et al. *Mater Sci Eng A* 2001;312:136.
- [88] Pryds NH, Eldrup M, Ohnuma M, Pedersen AS, Hattel J, Linderroth S. *Mater Trans JIM* 2000;41:1435.
- [89] Glade SC, Busch R, Lee DS, Johnson WL, Wunderlich RK, Fecht HJ. *J Appl Phys* 2000;87:7242.
- [90] Pekarskaya E, Löffler JF, Johnson WL. *Acta Mater* 2003;51:4045.
- [91] Sietsma J, Thijsse BJ. *Phys Rev B* 1995;52:3248.